Journal of Materials Science & Technology 179 (2024) 224–239

Contents lists available at ScienceDirect

Journal of Materials Science & Technology

journal homepage: www.elsevier.com/locate/jmst

Research Article

Optimization of the *in vitro* biodegradability, cytocompatibility, and wear resistance of the AZ31B alloy by micro-arc oxidation coatings doped with zinc phosphate

Chao Yang[a,g], Suihan Cui[a,b,*], Ricky K.Y. Fu[b], Liyuan Sheng[c,d,*], Min Wen[c], Daokui Xu[e], Ying Zhao[f], Yufeng Zheng[c], Paul K. Chu[b], Zhongzhen Wu[a,*]

[a] School of Advanced Materials, Peking University Shenzhen Graduate School, Shenzhen 518055, China
[b] Department of Physics, Department of Materials Science & Engineering, and Department of Biomedical Engineering, City University of Hong Kong, Tat Chee Avenue, Kowloon, Hong Kong 999077, China
[c] Shenzhen Institute, Peking University, Shenzhen 518057, China
[d] PKU-HKUST Shenzhen – Hong Kong Institution, Shenzhen 518057, China
[e] Key Laboratory of Nuclear Materials and Safety Assessment, Institute of Metal Research, Chinese Academy of Sciences, Shenyang 110016, China
[f] Shenzhen Institutes of Advanced Technology, Chinese Academy of Sciences, Shenzhen 518055, China
[g] National Engineering Research Center of Light Alloy Net Forming and State Key Laboratory of Metal Matrix Composite, Shanghai Jiao Tong University, Shanghai 200240, China

ARTICLE INFO

Article history:
Received 25 July 2023
Revised 7 September 2023
Accepted 10 September 2023
Available online 24 October 2023

Keywords:
Mg alloys
MAO coatings
Degradation regulation
Cytocompatibility
Wear resistance

ABSTRACT

As implanted bone fixation materials, magnesium (Mg) alloys have significant advantages because the density and elastic modulus are closest to those of the human bone and they can bio-degrade in the physiological environment. However, Mg alloys degrade too rapidly and uncontrollably thus hampering clinical adoption. In this study, a highly corrosion-resistant zinc-phosphate-doped micro-arc oxidation (MAO) coating is prepared on the AZ31B alloy, and the degradation process is assessed *in vitro*. With increasing zinc phosphate concentrations, both the corrosion potentials and charge transfer resistance of the AZ31B alloy coated with MAO coatings increase gradually, while the corrosion current densities diminish gradually. Immersion tests in the simulated body fluid (SBF) reveal that the increased zinc phosphate concentration in MAO coating decreases the degradation rate, consequently reducing the release rates of Mg^{2+} and OH^- in the physiological micro-environment, which obtains the lowest weight loss of only 5.22% after immersion for 56 days. Effective regulation of degradation provides a weak alkaline environment that is suitable for long-term cell growth and subsequent promotion of bone proliferation, differentiation, mineralization, and cytocompatibility. In addition, the zinc-phosphate-doped MAO coatings show an improved wear resistance as manifested by a wear rate of only 3.81×10^{-5} mm^3 N^{-1} m^{-1}. The results reveal a suitable strategy to improve the properties of biodegradable Mg alloys to balance tissue healing with mechanical degradation.

1. Introduction

Owing to accidents, injuries, and senile osteoporosis, the demand for implantable orthopedic fixation materials and medical devices is increasing [1–3]. Generally, the orthopedic fixation implant works temporarily, it has to be taken out after the bone repairing, which causes secondary surgery and great pain for the patient. Then, it is meaningful to develop a new biodegradable orthopedic implant that could disappear after bone repairing. Magnesium (Mg) alloys could biodegrade in the physiological environment thus eliminating the need for a second surgery to remove the implants [4–8]. Degradation of Mg alloys generates Mg^{2+} ions leading to local basification which can promote bone tissue healing [9–11]. More importantly, Mg alloys have a density and elastic modulus close to those of the human bones thus avoiding stress shielding and benefiting the osseointegration [12–15]. However, Mg alloys degrade rapidly *in vivo*, which leads to a loss of mechanical integrity and influences bone healing. Additionally, excessively accumulated H_2 and OH^- produced by rapid degradation may cause subcutaneous emphysema and alkalosis [16–18]. Therefore, it is

* Corresponding authors.
E-mail addresses: cuish@pku.edu.cn (S. Cui), lysheng@yeah.net (L. Sheng), wuzz@pkusz.edu.cn (Z. Wu).

https://doi.org/10.1016/j.jmst.2023.09.019
1005-0302/

crucial to optimize the biodegradation behavior of Mg alloys before their clinical application.

Among all methods to improve the biodegradation behavior of Mg alloy, micro-arc oxidation (MAO) has been thought as the most potential one, because of its convenient fabrication, in-situ formed ceramic coating, excellent shape adaptability, and so on [19–22]. Moreover, the MAO discharge breakdown process generates abundant three-dimensional pores suitable for the growth and proliferation of osteoblasts [23,24]. Conversely, the porous structure of the MAO coating also leads to the infiltration of the corrosion medium and decreases the effective protective time to around 300 h, which is much shorter than the required time for bone reconstruction of 100 days [25,26]. Mingo et al. [27] have incorporated hydroxyapatite nanotubes into the Mg alloy MAO coating to reduce the degradation rate and Gao et al. [28] have doped Mg alloy MAO coatings with ZrO_2 to reduce the corrosion current density by two orders of magnitude. Our previous work shows that doping with a large concentration of ZnO nanoparticles can extend the salt spraying lifetime of the coating to 2000 h [29]. Roknian et al. [30] have found that Zn not only improves the corrosion resistance of the MAO coating on the Mg alloy but also exhibits good biological functions because the release of Zn^{2+} ions improves the antibacterial properties and mitigates inflammation in the early stage after implantation. In order to further improve the corrosion resistance of Mg alloys, Iqbal et al. [31] have prepared Mg phosphate coatings on the Mg alloy, indicating that the ability of bone healing is enhanced by P [32,33]. Liu et al. [34] have prepared a phosphate-composite MAO coating on the Mg alloy to reduce the degradation rate and improve bone healing and Wu and co-workers [35] have doped the Mg alloy with both Zn and P. The salt spraying lifetime is extended to 4200 h which is adequate for clinical application. It can be concluded that doping with a suitable concentration of desirable elements in MAO coatings can improve biodegradation behavior and promote tissue regeneration. However, infiltration and pitting would inevitably happen due to the relative porous structure of MAO coatings. As a result, the generation of hydrogen gas and corresponding loose corrosion products along the coating/alloy interface is prone to causing peeling failure [36]. In addition, in the context of bone fixation implants, the presence of fretting wear during initial implantation and stress loading can further intensify the detachment of MAO coating [37]. Therefore, reasonable self-sealing and wear resistance are important requirements for the MAO coating that could ensure its protecting effect on the implant.

Herein, the zinc phosphate was chosen as the anti-corrosion additive and MAO coatings with different concentrations of zinc phosphate were prepared on the AZ31 Mg alloy in the present research. The microstructure, electrochemical properties, degradation behavior, cytocompatibility, and wear resistance of the MAO coatings were investigated to systematically evaluate the reasonable zinc phosphate addition. The results could help to understand the feasibility of zinc-phosphate-doped MAO coatings for Mg-based bone fixation implants.

2. Experimental details

2.1. Materials

The Mg alloy (AZ31B with σb ranging from 225 to 235 MPa, $\sigma s_{0.2}$ ranging from 145 to 150 MPa, and δ ranging from 12% to 14%, 200 mm × 100 mm × 1 mm) plate was purchased from Guanyue Metal Materials Co., Ltd. (Dongguan, China). The specimens for corrosion and biological tests with size of 10 mm × 10 mm × 1 mm and specimens for tribological tests with size of 30 mm × 30 mm × 1 mm were cut from the as-received Mg alloy plate, respectively. The chemical reagents including acetone, anhydrous ethanol, sodium hydroxide, and hydrated zinc acetate of analytical purity were obtained from China National Pharmaceutical Group Chemical Reagent Co., Ltd. (Shanghai, China). The other reagents such as sodium hexametaphosphate and sodium fluoride were analytical grade and purchased from Guangdong Xilong Chemical Co., Ltd. (Shantou, China). The simulated body fluid (SBF solution) was purchased from Kondisi Chemical Co., Ltd. (Hubei, China) and the 1500-grit sandpaper was purchased from 3 M China Co., Ltd. (Shanghai, China). All the reagents were used without further purification.

2.2. Preparation of MAO coatings

The Mg alloy specimens with different sizes were polished with 1500-grit sandpaper, cleaned sequentially with deionized water, anhydrous ethanol, and acetone ultrasonically for 30 min, and dried before conducting MAO. The preparation process of the MAO coatings is illustrated in Fig. 1. A MgF_2/MgO passivation layer was prepared in an alkaline electrolyte and then a zinc phosphate-doped MAO coating was produced in the Zn-containing electrolyte. The alkaline MAO electrolyte was prepared by mixing 20 g L^{-1} sodium hexametaphosphate, 3 g L^{-1} sodium hydroxide, and 5 g L^{-1}

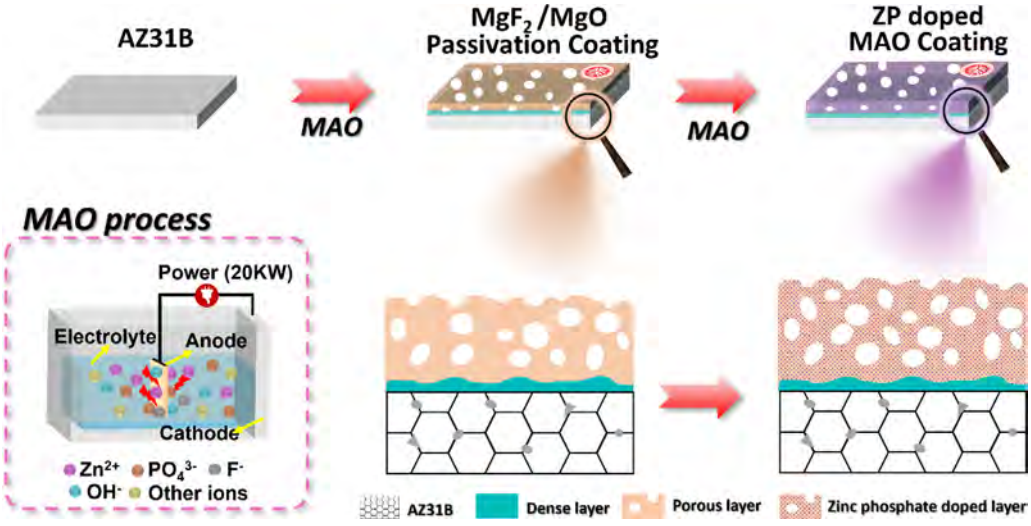

Fig. 1. Schematic diagram illustrating the preparation of zinc phosphate-doped MAO coatings on the Mg alloy specimen.

sodium fluoride at a rate of 400 r min^{-1} for 2 h until the chemicals dissolved fully in deionized water. The Zn-containing electrolyte for MAO coating preparation contained 20 g L^{-1} sodium hexametaphosphate, 5 g L^{-1} sodium fluoride, and 0/5/10/15 g L^{-1} zinc acetate hydrate, and the coated specimens were labeled as Zn-0, Zn-1, Zn-2, and Zn-3, respectively. During MAO, a 20 kW bipolar pulse power supply was used in the constant current mode with the Mg alloy being the anode and the stainless steel container as the cathode. The preparation parameters were a current density of 5.5 A dm^{-2}, frequency of 200 Hz, duty cycle of 12%, reaction time of 15 min (10-min reaction with the alkaline electrolyte, followed by a 5-min reaction with the zinc-containing electrolyte.), and electrolyte temperature below 40 °C.

2.3. Characterization

The microstructure of the MAO coating was examined by field-emission scanning electron microscopy (FESEM, Carl Zeiss, SUPRA® 55) and the chemical composition was determined by energy-dispersive X-ray spectroscopy (EDS, Oxford X-Max 20). X-ray diffraction (XRD, Bruker, D8 Advance) was performed to determine the crystal structure using a Cu target ($\lambda = 0.15418$ nm) as the X-ray source at a scanning rate of 5°/min, step size of 0.05 s, and diffraction angle 2θ range of 10°–80°. A focused ion beam (FIB, Scios, FEI) was used to cut the surface and cross-sections prior to high-resolution transmission electron microscopy (HRTEM: JEM-3200FS, Japan). 3D laser confocal scanning microscopy (LCSM, VK-X200 series, Oxford, X-Max20, England) was conducted to test the 3D profile of the sample. The coating thickness was determined by SEM image of the coating cross-section. The surface roughness of the sample was assessed by a surface roughness tester (JD220, JitaiKeyi, China). Five measurements were made to determine the averages.

2.4. Corrosion resistance

The corrosion resistance of the Mg alloy specimens without and with MAO coatings was determined in the simulated body fluid (SBF) on the electrochemical workstation (NPROBE/EPC42, Zahner, Germany) with a three-electrode cell system. The testing temperature was 37 °C and an area of 2.4 cm^2 was exposed on the working electrode. A saturated calomel electrode (SCE) was the reference electrode and Pt served as the counter electrode. The specimen was left at the open circuit potential (OCP) for 30 min in SBF to ensure system stability and polarization curves (Tafel) were acquired at a scanning rate of 1 mV s^{-1}. The corrosion potential E_{corr} (V) and corrosion current density i_{corr} (A cm^{-2}) were obtained by extrapolating the Tafel curve. The former was the intersection potential of the cathodic and anodic curves and the latter was the intersected current density of the cathodic and anodic curves. The impedance spectra (EIS) were acquired with a sinusoidal signal of 10 mV in the frequency range of 100 kHz to 100 mHz, and analyzed and fitted by the ZsimpWin software. During the fitting process, the variance of the impedance spectra was less than 0.01 and the standard deviation was within 10% to ensure good reliability. The immersion experiment was performed in a 50 mL centrifuge tube. After immersion in 30 mL of SBF at 37 °C for 3, 7, 14, 28, and 56 days, the specimens were removed, washed with water and ethanol, and dried. Ultrasonic cleaning removed the corrosion products from the AZ31B alloy coated with MAO coatings to determine the mass loss. The corrosion products of AZ31B alloy were removed with a chromate acid solution ($CrO_3 + AgNO_3$) before weight measurement. The pH value of the immersion solution at different times was measured by a pH meter (PHBJ-260, Shanghai Yidian). The ion concentration in the SBF was determined by inductively coupled plasma atomic emission spectrometry (ICP-AES, JY2000–2, HORIBA JOBINYVON).

2.5. Biological assessment

The cell skeleton and DAPI staining were conducted. The specimens were sealed with silicone gel leaving only the tested surface exposed. They were sterilized with dry heat at 150 °C for 3 h and then soaked in anhydrous ethanol. Mouse osteoblasts MC3T3-E1 were seeded at a density of 5×10^4 cells per well and the cell suspension was spread evenly. The cells were incubated for 1, 5, and 24 h. After incubation, the culture medium was removed and the samples were washed twice with the Phosphate Buffered Saline (PBS) buffer by shaking. The samples were then fixed with the PBS buffer containing 7% formaldehyde at room temperature for 5 min. They were aspirated and then washed twice with PBS. 0.1% TritonX-100 was added for 5–8 min to disrupt the cell membrane and then washed three times with the PBS buffer after the supernatant was removed. The 165 nM RGD peptide was added and incubated in the dark at 25 °C for 40 min. After removing the staining solution, the samples were washed three times with the PBS buffer, and stained with the DAPI fluorescent staining solution at 25 °C for 3–5 min. Finally, the PBS buffer was added prior to fluorescence microscopy.

The cell toxicity was evaluated. The non-testing surfaces were sealed with silicone gel and sterilized by dry heat at 150 °C for 3 h followed by soaking in anhydrous ethanol. The bone marrow mesenchymal stem cells (BMSCs, ATCC®PCS-500–012™) were cultured in the medium (α-MEM, 10% fetal bovine serum, 1% penicillin and streptomycin). The materials were extracted from the culture medium with a concentration of 1 mL cm^{-2} for 3 days under 5% CO_2 and 37 °C, filtered through a 0.22 μm filter, and diluted to 80%, 60%, and 40%, respectively. The cultured BMSC cells were co-cultured with the extraction solution at a density of 2000 cells per well on a 96-well plate. The extraction solution was replaced after cultivation for 1 day, and the cell viability was assessed using Alamar Blue after cultivation for 3 days. The cell toxicity was evaluated according to ISO10993–5. The negative control was the group without the extraction solution, and the positive control was the group with the cells cultured with 10% dimethyl sulfoxide solution.

The lactate dehydrogenase (LDH) expression tests were conducted on the cells co-cultured on the specimens to analyze the cell proliferation. The non-testing surfaces were sealed with silicone gel, sterilized by dry heat at 150 °C for 3 h, and soaked in anhydrous ethanol. The BMSCs cells were seeded on the samples with a density of 1.5×10^5 cells per well on 96-well plates with the α-MEM culture medium. The cells were cultured under 5% CO_2 at 37 °C for 1 day and transferred to a new well plate. The culture medium containing the osteogenic induction solution was refreshed every other day. Subsequently, the cell culture plates were centrifuged at 400 g for 5 min using a multi-well plate centrifuge. The supernatant was removed and 150 μL of LDH reagent was added from the kit and diluted 10-fold with PBS. Mixed cells were gently shaken and after further incubation for 1 h, the cell culture plates were centrifuged for 5 min. 120 μL of supernatant from each well was added to the corresponding wells of the new plate to make immediate sample measurements. The expression levels of LDH were measured on the cells co-cultured on the specimens for 1, 3, and 7 days.

The alkaline phosphatase (ALP) expression tests were conducted. The non-testing surfaces were sealed with silicone gel, sterilized by dry heat at 150 °C for 3 h, and soaked in anhydrous ethanol. The bone marrow mesenchymal stem cells (BMSCs) were resuspended, counted, and prepared with a density of 1.5×10^5 cells per well on 96-well plates with the α-MEM culture medium.

The cells were cultured under 5% CO_2 at 37 °C for 1 day and transferred to a new well plate. The culture medium containing the osteogenic induction solution was refreshed every other day and the expression levels of ALP were measured after cultivation for 7 and 14 days.

2.6. Tribological evaluation

The friction and wear tests were carried out on a friction and wear tester (MFT-5000, Rtec instruments, USA) at room temperature. A 4 mm diameter Si_3N_4 ceramic ball was selected as the counter surface with a rotation diameter of 5 mm and rotation speed of 100 r min^{-1}. The wear of the coating under a 3 N load after 60 min was determined to measure the tribological properties. The actual wear rate was calculated by Eq. (1):

$$W = V/(F \times t \times 2pnr) \quad (1)$$

where V (mm^3) is the wear volume, F (N) is the load force, t (s) is the actual wear time, n (m s^{-1}) is the rotation speed, and r (m) is the rotation radius. Five points were tested to obtain the average values.

3. Results and discussion

3.1. Characterization

Fig. 2(a) shows the variation of the voltage with time during MAO. The actual voltage increases gradually, which indicates that the insulating coating becomes thick and enhances the resistance. The discharge process can be divided into three stages. In the first stage (0–180 s), a dense passivation film is created rapidly on the AZ31B alloy and the ions in the solution accumulate on the passivation layer causing a rapid increase in the voltage. In the second stage (180–600 s), the voltage gradually increases until the weak points in the coating are broken down, resulting in dense white arcs as shown in Fig. 2(b). At high temperature and pressure, the molten metal in the discharge channel is sprayed out to react with the solution and finally condense into the coating. Consequently, the coating thickens gradually, resulting in a gradually increasing breakdown voltage, which promotes the generation of larger and brighter arcs (Fig. 2(b)). In the third stage (600–700 s), the alkaline electrolyte is replaced by the Zn-containing electrolyte, showing a sharp increase in the discharge voltage. Both the number and size of the arcs decrease with the color changing from white to yellow (Fig. 2(b)). This is mainly attributed to the rapid re-accumulation of ions on the coating. Subsequently, as the voltage increases slowly, the coating continues thickening. Moreover, the discharge voltage increases with the increase of Zn salt concentration.

Fig. 2(c) shows the surface morphology of the undoped MAO coating on the AZ31B alloy. Volcano-like pores with different sizes and apertures are distributed randomly on the surface. The Zn-1 coating prepared with 5 g L^{-1} Zn salt exhibits a larger pore size, because the Zn salt enhances the discharge, thus giving rise to a higher discharge voltage and larger arcs (Fig. 2(d)). However, as the Zn salt concentration goes up, the pore size of the Zn-2 and Zn-3 coatings decreases, because more Zn compounds are generated and backfill the pores (Fig. 2(e, f)). Besides, the arc discharge is enhanced, resulting in larger coating roughness as revealed by LCSM shown in Fig. S1 and Table S1 in the Supplementary Material. However, we did not further increase the concentration of zinc acetate is due to the MAO discharge with a higher content of Zn salt in the later stage will be too intense, which can easily lead to coating erosion and failure.

The cross-sectional morphology and EDS results of the coatings are shown in Fig. 3. With increasing the Zn concentration, the coating thickness increases only slightly due to a slight decrease in the conductivity of the electrolyte [35]. As a result, the thicknesses of the Zn-0, Zn-1, Zn-2, and Zn-3 coatings are 41.5 ± 3.7, 44.1 ± 3.6, 45.4 ± 3.1, and 47.3 ± 4.2 μm, respectively (Table S1), which are consistent with the variation trend of the discharge voltage. The EDS elemental maps reveal that all the elements (O, F, Mg, and P) are relatively uniformly distributed except Zn which prefers to aggregate near the pores. Especially the Zn-3 coating, the aggregation of Zn is more obvious, due to its higher Zn content.

Fig. 4(a) shows the phase constitute of the MAO coatings. Compared with the AZ31B substrate, the MAO coatings show weaker diffraction peaks in the range of 30°–75° (PDF#35–0821). The Zn-0 coating exhibits peaks of the MgF_2 (111) plane (PDF#38–0882) and typical peaks of the MgO (111) plane (PDF#45–0946) at 32.3° and 36.9°, respectively. With the addition of Zn content, diffraction peaks of the $Zn_3(PO_4)_2$ along (101), (021), (121), and (130) crystallographic planes emerge at 22.1°, 27.5°, 30.6°, and 33.7°, respectively (PDF#30–1490). Moreover, the broad peak feature also indicates that there would be a large amount of amorphous phase.

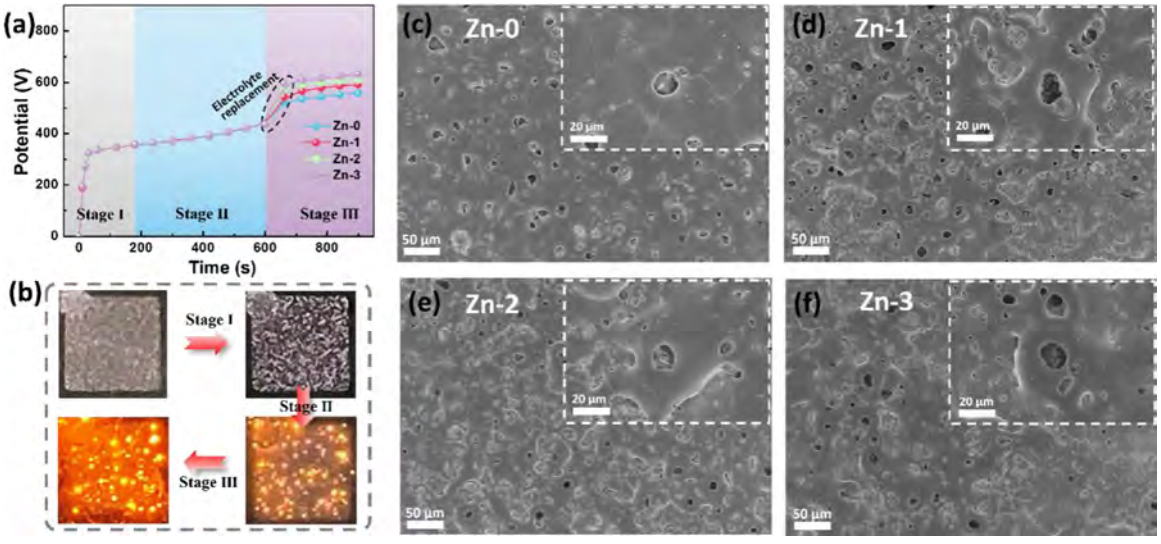

Fig. 2. Fabrication and characteristics of zinc phosphate-doped MAO coatings: (a) Voltage–time curve; (b) Arc evolution; (c–f) SEM micrographs of coatings prepared in different solutions (Insets showing the magnified features).

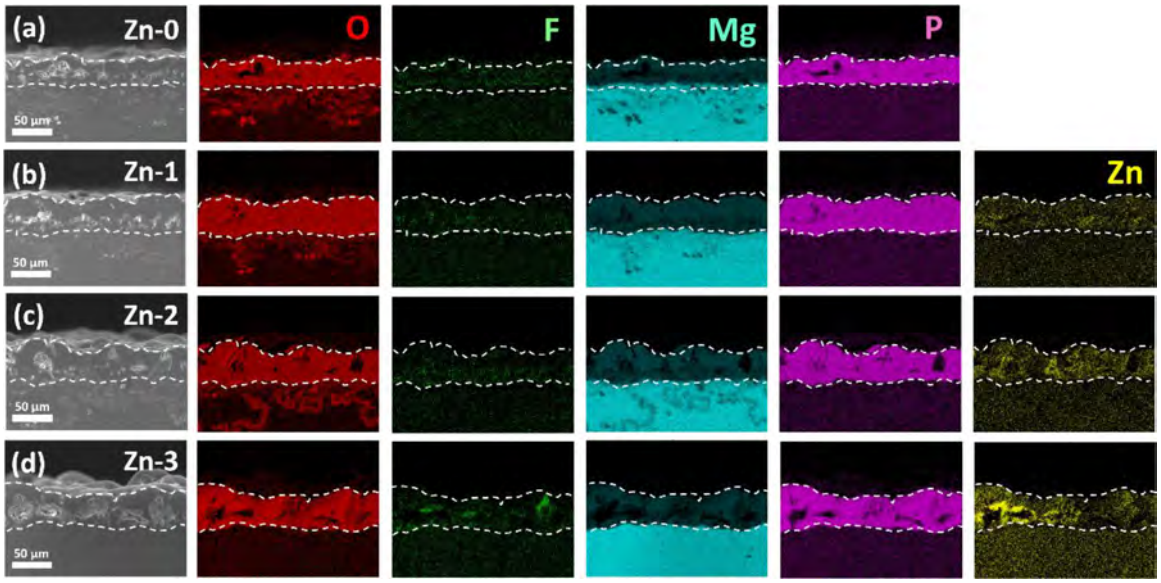

Fig. 3. Cross-sectional SEM images of MAO coatings and corresponding EDS elemental distributions: (a) Zn-0, (b) Zn-1, (c) Zn-2, and (d) Zn-3.

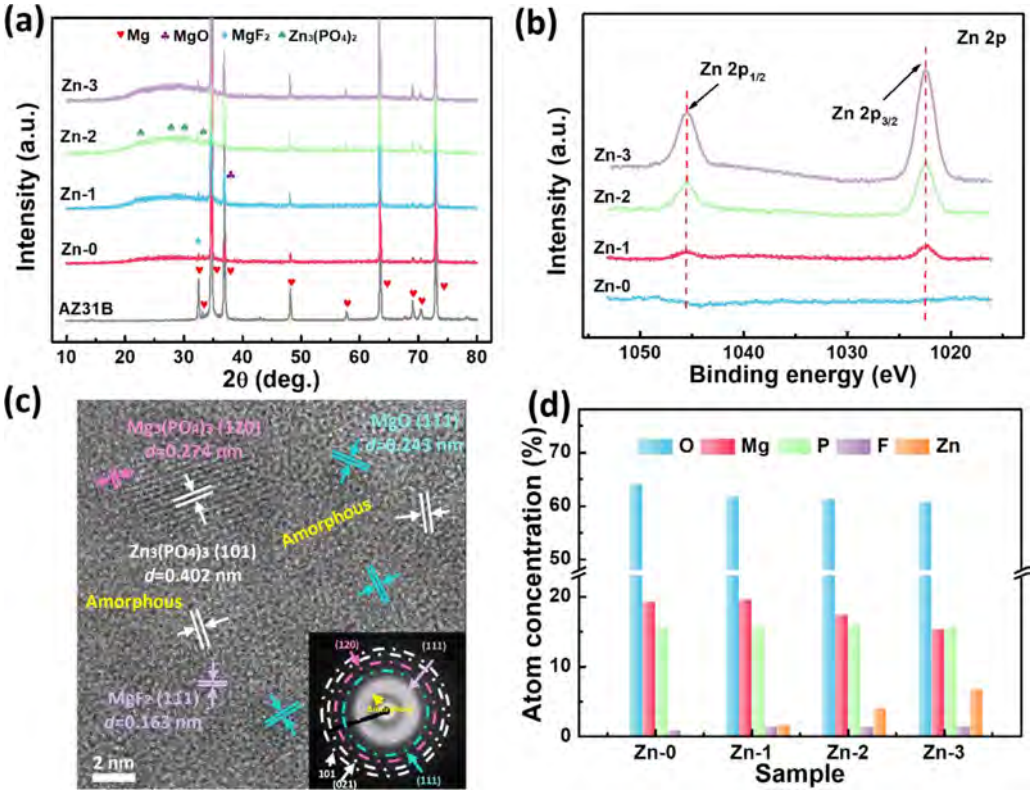

Fig. 4. Phase and chemical composition of the MAO coatings specimens doped with different concentrations of zinc phosphate: (a) XRD patterns; (b) XPS of Zn 2p spectra; (c) HRTEM image of Zn-3; (d) Chemical composition.

XPS confirms the presence of Mg, P, Zn, O, F, and C. Carbon is a contaminant due to air exposure (Fig. S2). The Zn 2p spectrum shows peaks at 1022.9 eV and 1044.8 eV, corresponding to Zn $2p_{3/2}$ and $2p_{1/2}$, respectively, indicating the Zn divalent state [38,39]. With increasing the Zn concentration in the electrolyte, the intensity of the Zn 2p spectrum gradually increases (Fig. 4(b)). The O 1s peak of the AZ31B alloy coated with MAO coatings shifts gradually to higher binding energies, indicating the generation of more oxide species. The fitted O 1s peak of Zn-3 shows peaks at 531.9 eV and 533.6 eV corresponding to Mg-O in MgO and P-O-Zn and P-O-Mg in phosphate, respectively, whereas that at 532.7 eV is associated with H–O bond of water or hydroxide from air (Fig. S2(d)) [40–42]. XRD and XPS analyses show that the main phases in the MAO coatings are MgO, MgF_2, $Mg_3(PO_4)_2$, $Zn_3(PO_4)_2$, and amorphous phases. HRTEM observations on Zn-3 coating demonstrate the presence of MgO (111), MgF_2 (111), $Mg_3(PO_4)_2$ (120), and $Zn_3(PO_4)_2$ (021) facets in the form of nanocrystals which are randomly distributed in the amorphous phase of MgO (Fig. 4(c)). It is worth noting that no diffraction peaks of $Mg_3(PO_4)_2$ could be detected in XRD, but a small amount of $Mg_3(PO_4)_2$ was ob-

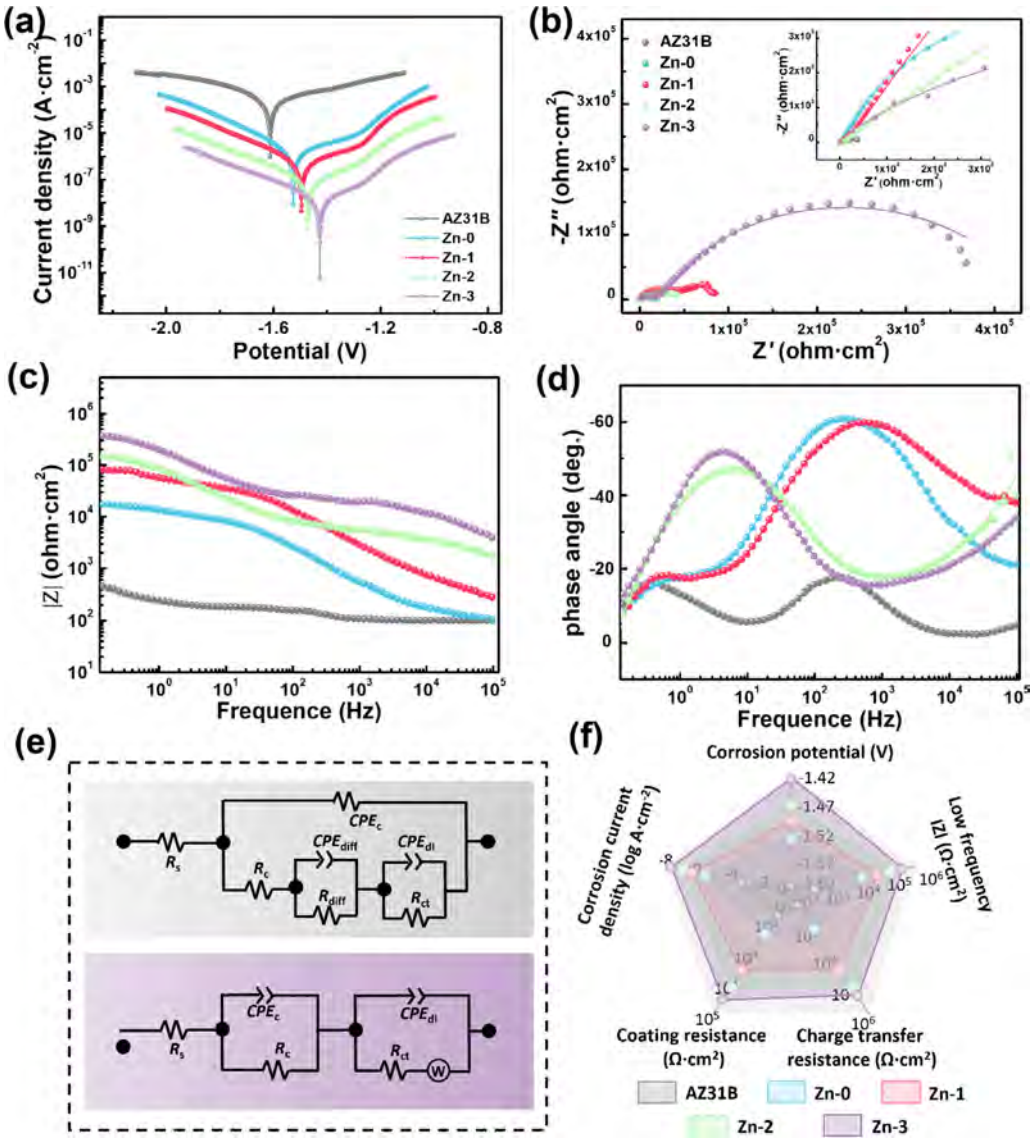

Fig. 5. Electrochemical properties of the AZ31 alloy substrate and MAO coatings doped with different concentrations of zinc phosphate: (a) Tafel plot; (b–e) EIS plots; (b) Nyquist plots; (c) Bode-impedance plots; (d) Bode-phase angle plots; (e) Equivalent circuits; (f) Pentagonal illustration.

served in HRTEM. It can be deduced that $Mg_3(PO_4)_2$ may primarily exist in an amorphous form, with only a small amount existing in nanocrystalline form. EDS shows that all the elements are distributed uniformly and with increasing Zn salt concentration in the electrolyte, the Zn concentration in the coatings increases. The Zn concentration in Zn-3 is 6.83 at%, which is the largest among all the samples (Fig. 4(d)).

3.2. Electrochemical properties in SBF

Electrochemical tests are conducted in SBF to evaluate the corrosion resistance of the AZ31B alloy and Zn-0, Zn-1, Zn-2, and Zn-3 coatings. The Tafel results in Fig. 5(a) and Table 1 reveal that the corrosion potentials increase from −1.612 V (AZ31B) to −1.526 V (Zn-0) after MAO and then increase gradually to −1.496 V (Zn-1), −1.470 V (Zn-2), and −1.427 V (Zn-3). The corrosion current densities decrease from 2.228×10^{-4} A cm^{-2} to 1.436×10^{-6} A cm^{-2}, 4.832×10^{-7} A cm^{-2}, 7.834×10^{-8} A cm^{-2}, and 1.413×10^{-8} A cm^{-2} for Zn-0, Zn-1, Zn-2, and Zn-3, respectively, with the maximum reduction larger than four orders of magnitude. This can be attributed to the protective effect of the MAO coatings, which improves corrosion resistance.

Table 1
Corrosion potentials and corrosion current densities of the AZ31B alloy substrate and MAO coatings doped with different concentrations of zinc phosphate.

Specimens	Corrosion potentials (V)	Corrosion current densities (A cm^{-2})
AZ31B	−1.612	2.228×10^{-4}
Zn-0	−1.526	1.436×10^{-6}
Zn-1	−1.496	4.832×10^{-7}
Zn-2	−1.470	7.834×10^{-8}
Zn-3	−1.427	1.413×10^{-8}

EIS is conducted to analyze the corrosion resistance of the AZ31B alloy and AZ31B alloy coated with MAO coatings in SBF. Fig. 5(b) shows that all the specimens exhibit an obvious capacitive behavior during immersion. Generally, the diameter of the second capacitor loop of the MAO coating at low frequency reflects the final corrosion resistance performance of the coating. Compared with the AZ31B alloy, the diameter of the capacitive loop

Table 2
Fitted EIS data of the AZ31B alloy substrate and MAO coatings doped with different concentrations of zinc phosphate.

Specimens	AZ31B	Zn-0	Zn-1	Zn-2	Zn-3
CPE_c (ohm^{-1} cm^{-2} s^n)	2.419×10^{-4}	5.770×10^{-5}	1.364×10^{-8}	8.704×10^{-9}	5.868×10^{-9}
n_c	0.8831	0.1219	0.7670	0.9486	0.9445
R_c (ohm cm^2)	88.97	3.530×10^2	6.480×10^3	1.516×10^4	3.484×10^4
CPE_{diff} (ohm^{-1} cm^{-2} s^n)	2.656×10^{-3}	3.697×10^{-4}	3.940×10^{-7}	2.128×10^{-8}	1.023×10^{-8}
n_{diff}	0.8562	0.2309	0.7373	0.3222	0.7630
R_{diff} (ohm cm^2)	46.10	4.758×10^2	5.603×10^3	7.732×10^4	4.138×10^5
CPE_{dl} (ohm^{-1} cm^{-2} s^n)	2.940×10^{-3}	1.221×10^{-5}	8.329×10^{-6}	4.158×10^{-7}	2.548×10^{-7}
n_{dl}	1.000	0.8559	0.9227	0.7598	0.4077
R_{ct} (ohm cm^2)	1.814×10^2	1.406×10^3	4.275×10^4	1.583×10^5	2.624×10^5

at low frequency for the MAO coating increases gradually with increased zinc phosphate concentration, indicating gradual improvement in the corrosion resistance. Generally, the impedance modulus at low frequencies in the Bode impedance plot reflects the overall impedance. The low-frequency impedance of Zn-0 increases from 4.857×10^2 ohm cm^2 to 1.741×10^4 ohm cm^2, which is nearly two orders of magnitude larger than that of the AZ31B substrate. The low-frequency impedances of Zn-1, Zn-2, and Zn-3 increase to 8.543×10^4, 1.476×10^5, and 3.801×10^5 ohm cm^2, respectively (Fig. 5(c)).

The EIS results are fitted with equivalent circuits (ECs) by the complex nonlinear least-square method. The circuits in Fig. 5(e) are determined based on the time constant in the Bode phase angle plot in Fig. 5(d). The relaxation processes of AZ31B alloy at medium-high and low frequencies correspond to the 3–5 nm MgO passive film and the metal interface. The capacitance circuit in the high-frequency or medium-frequency region is related to the MAO coating, and the electrochemical behavior in the low-frequency region is determined by the interfacial reaction between the coating and Mg alloy substrate in SBF. Owing to the nonuniformity caused by the rough porous coatings with heterogeneous chemical composition, the charge transfer process cannot be analyzed based on the ideal capacitor or resistor [43]. Therefore, a constant phase element (CPE) expressed by Eq. (2) is chosen to describe the non-ideal resistance and capacitance of the coating [44]:

$$Z_{CPE} = \frac{1}{T(j\omega)^n} \quad -1 \le n \le 1 \tag{2}$$

where Z_{CPE} is the resistance of the CPE, T is the CPE coefficient, n is the CPE index, $j = \sqrt{-1}$ is the imaginary unit, and ω is the angular frequency (related to the frequency f, $\omega = 2\pi f$). When n is equal to 1, –1, and 0, the CPE is simulated as an ideal capacitor, ideal inductor, and ideal resistor, respectively. The EIS data of the AZ31B alloy and AZ31B alloy coated with MAO coatings are fitted with the capacitance circuit, while the Zn-3 coating is fitted by adding a Weber resistor. Here, CPE_c and R_c represent the capacitance and resistance of the passive film or MAO coating on the AZ31B substrate, CPE_{diff} and R_{diff} represent the diffusion capacitance and resistance of the specimen in the SBF solution, and CPE_{dl} and R_{ct} are the double-layer capacitance and charge transfer resistance in the Faraday process, respectively.

Table 2 shows the variation of the CPE coefficients and resistances of the AZ31B alloy and coatings in SBF. After MAO, the CPE_{dl} values decrease from 2.94×10^{-3} ohm^{-1} cm^{-2} s^n to 1.221×10^{-5} ohm^{-1} cm^{-2} s^n for the Zn-0 coating. With increasing zinc phosphate concentration, the CPE_{dl} values decrease further to 8.329×10^{-6}, 4.158×10^{-7}, and 2.548×10^{-7} ohm^{-1} cm^{-2} s^n for Zn-1, Zn-2, and Zn-3, respectively. Meanwhile, the CPE_c values decrease from 2.419×10^{-4} ohm^{-1} cm^{-2} s^n for AZ31B to 5.770×10^{-5}, 1.364×10^{-8}, 8.704×10^{-9}, and 5.868×10^{-9} ohm^{-1} cm^{-2} s^n for Zn-0, Zn-1, Zn-2, and Zn-3, respectively. The CPE_{diff} values show a similar variation trend. Conversely, the resistance exhibits an opposite tendency. The R_{ct} values of AZ31B increase from 1.814×10^2 ohm cm^2 to 1.406×10^3 ohm cm^2 for the Zn-0 coating. With increasing the zinc phosphate concentration, the R_{ct} values increase gradually to a maximum of 2.624×10^5 ohm cm^2 for Zn-3. The R_c and R_{diff} values also show the same increasing trend with R_{ct}, indicating that the MAO coating forms a physical barrier to block the erosion and penetration of the SBF solution to the Mg alloy substrate. Meanwhile, doping with zinc phosphate weakens the charge transfer process of the corrosion anions in the SBF, thus resisting the corrosion of the corrosive medium in the weak holes and improving the corrosion resistance. The five sets of electrochemical data including the corrosion current density, corrosion potential, coating resistance, charge transfer resistance, and low-frequency resistance are compared in the pentagonal coordinate system and Zn-3 has the best corrosion resistance (Fig. 5(f)).

3.3. Degradation in SBF

To investigate the corrosion resistance mechanism, EIS is performed on the specimens after immersion for different time. As shown in Fig. 6(a1), the AZ31B alloy exhibits an obvious capacitive behavior, showing a gradual increase in the diameter of the capacitive loop with immersion time. However, the diameter of the capacitive loop decreases suddenly after immersion for 56 days, and an inductive loop appears simultaneously in the low-frequency region, indicating that the Mg alloy has been corroded. The Bode impedance plot of AZ31B shows the same trend in low-frequency impedance as shown in Fig. 6(a2). Compared to the situation before immersion, the low-frequency impedance of the AZ31B alloy increases to 1.196×10^3, 5.011×10^3, 5.103×10^5, and 1.208×10^6 ohm cm^2 after immersion in SBF solution for 3, 7, 14, and 28 days, respectively, but decrease to 7.156×10^4 ohm cm^2 after continuous immersion for 56 days. The Bode phase angle data in Fig. 6(a3) show that the peak of the phase angle shifts with immersion time, indicating that rapid corrosion has taken place. The increase in the capacitance and impedance in the early stage of immersion arises from the generation of corrosion products that cover the surface of the Mg alloy. However, corrosion leads to the dissolution of corrosion products in the later stage of the immersion, consequently accelerating the corrosion and penetration of SBF to the Mg alloy substrate.

With increasing the immersion time, the Nyquist data and Bode impedances of Zn-0 show a similar trend as the AZ31B alloy, except that there is no inductive behavior which represents the severe corrosion after 56 days. The diameter of the capacitive loop is larger than that of the AZ31B alloy (Fig. 6(b1, b2)). The peak of the Bode phase angle shows almost no shift in the early stage of immersion but shifts on a larger scale after immersion for 56 days. Hence, the corrosion reaction is slow in the early stage and fast in the later stage (Fig. 6(b3)). After doping with zinc phosphate, Zn-1 shows a smaller diameter of the capacitive arc and low-frequency impedance after immersion for 14 days due to smaller corrosion and fewer corrosion products in the early stage. As time

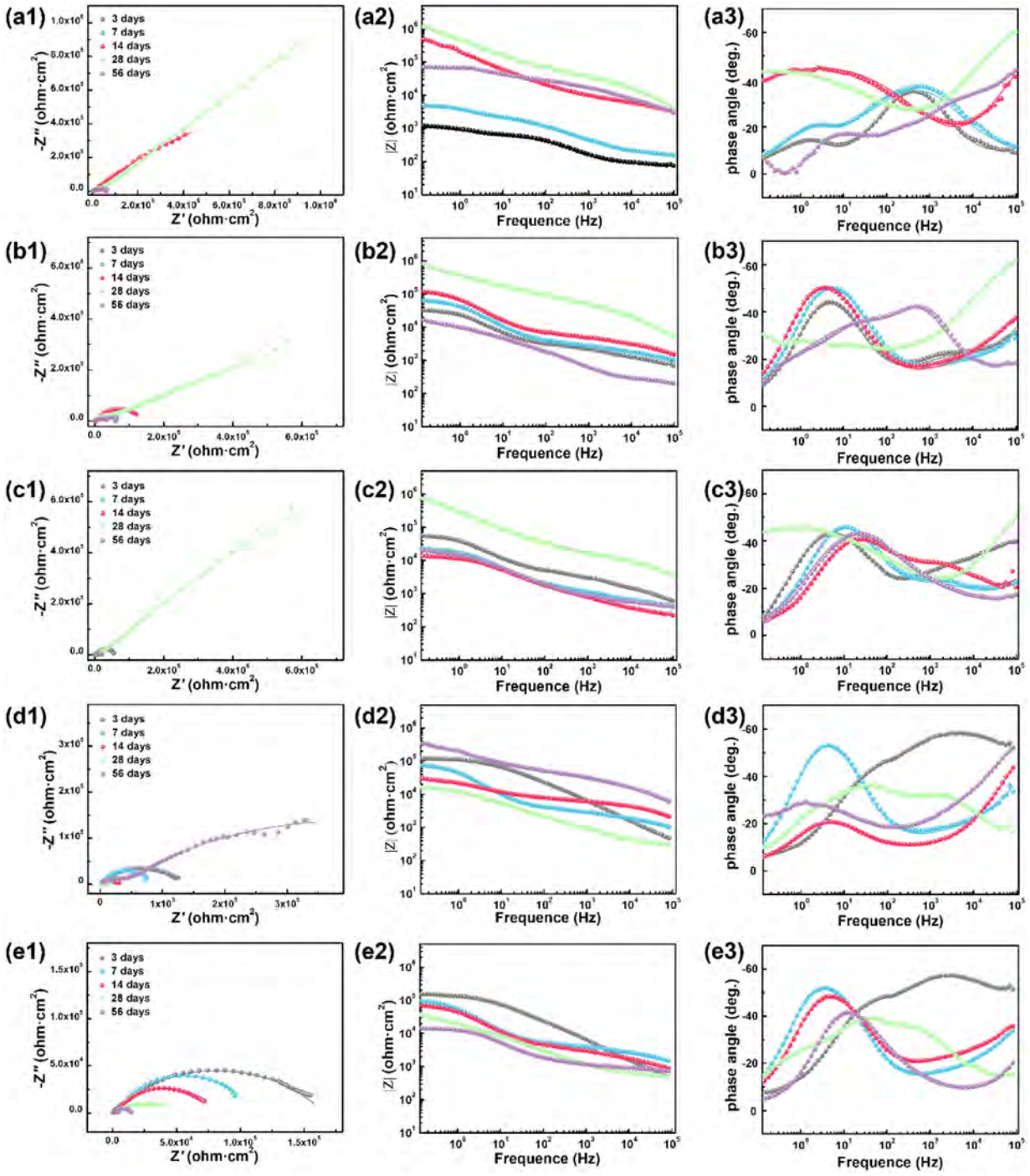

Fig. 6. EIS data of AZ31B alloy substrate and MAO coatings doped with different amounts of zinc phosphates after immersion in SBF for different time durations: (a1–a3) AZ31B, (b1–b3) Zn-0, (c1–c3) Zn-1, (d1–d3) Zn-2, and (e1–e3) Zn-3.

elapses, more corrosion products are generated, which results in the increase of capacitive arc and low-frequency impedance after 28 days. However, the capacitive arc and low-frequency impedance decrease again after 56-day immersion, because of the insufficient long-term corrosion resistance, resulting in severe corrosion in the later stage (Fig. 6(c)). The peak of the Bode phase angle in Fig. 6(c3) shifts during immersion, indicating that doping with zinc phosphate changes the corrosion reaction between the MAO coating and SBF. Zn-2 doped with more zinc phosphate shows a similar trend as Zn-1. After immersion for 56 days, the corrosion resistance of Zn-2 improves due to the generation of more corrosion products (Fig. 6(d)). In comparison, the capacitance arc and low-frequency impedance of Zn-3 don't show an increase and then decrease trend but continue to decrease within 56-day immersion, which implies that fewer corrosion products are generated and the corrosion resistance of the coating is better (Fig. 6(e)).

Based on the ECs determined from the Bode phase angle plot in Fig. 6, the EIS results are fitted and shown in Tables S2–S6. Fig. 7 shows the variations of the interface transfer resistance R_{ct}, coating resistance R_c, constant phase element coefficient CPE_{dl}, and coating constant phase element coefficient CPE_c in the corresponding EC diagrams. Fig. 7(a) exhibits that both the AZ31B alloy and Zn-

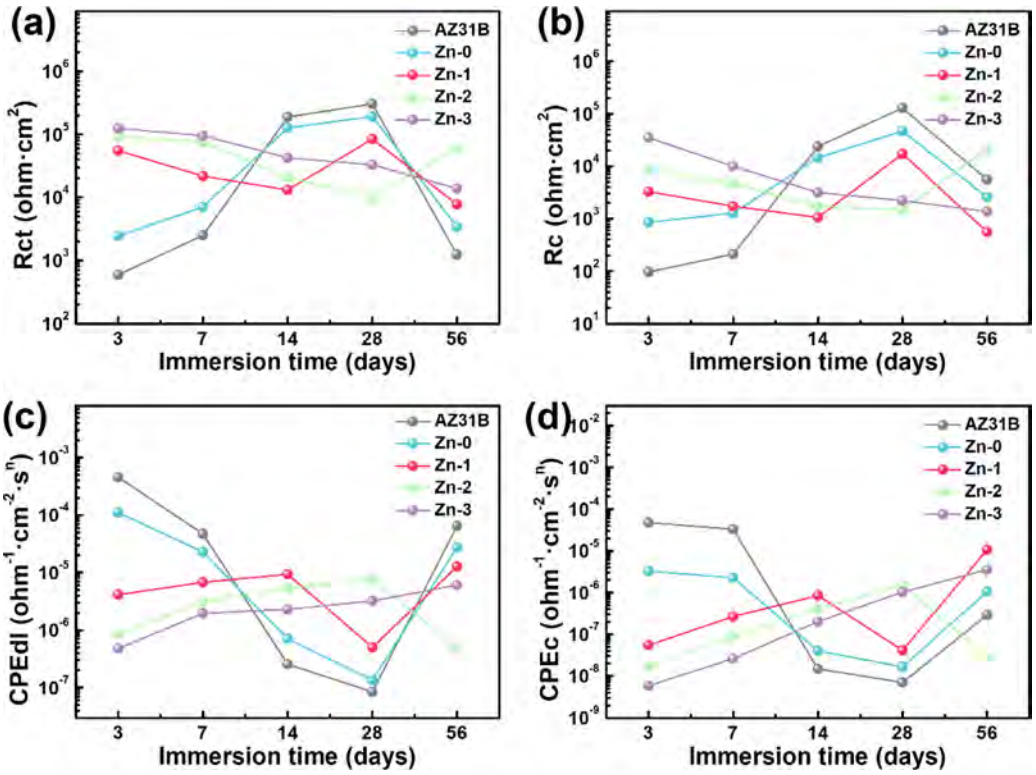

Fig. 7. Variations of electrical components in the equivalent circuits of the AZ31 alloy substrate and MAO coatings doped with different concentrations of zinc phosphate: (a) R_{ct}, (b) R_c, (c) CPE_{dl}, and (d) CPE_c.

0 have larger R_{ct} before immersion for 28 days and R_{ct} decreases after immersion for 56 days. Specifically, the AZ31B alloy shows a larger amplitude in the early stage and a smaller decreasing amplitude in the later stage, indicating that more corrosion products generated in the early and middle stages of immersion could accumulate on the surface and protect the alloy from rapid corrosion. However, the main component in the MAO coatings is MgO which exhibits a smaller activity than the Mg alloy, resulting in less corrosion and degradation. The R_{ct} values of the coatings doped with different concentrations of zinc phosphate decrease gradually in the first 14 days. However, the R_{ct} values of Zn-1 and Zn-2 turn upward after immersion for 28 and 56 days, while that of Zn-3 coating continues decreasing. In comparison, the variation of R_c is consistent with that of R_{ct}, while CPE_{dl} and CPE_c show an opposite trend, indicating that zinc phosphate plays a role in regulating the degradation rate of the AZ31B alloy coated with MAO coatings. Dissolution of zinc phosphate during immersion allays the rapid degradation of active MgO in the coating and generation of corrosion products. When the concentration of zinc phosphate is small, the effect is limited, resulting in the failure by severe corrosion in the later stage. With increasing the zinc phosphate content, the effect is enhanced. After immersion for 56 days, Zn-3 does not show the phenomenon and zinc phosphate regulates the degradation rate of the Mg alloy.

Fig. 8 shows the surface corrosion morphologies of the AZ31B alloy and AZ31B alloy coated with MAO coatings after immersion in SBF for 7, 28, and 56 days. As shown in Fig. 8(a1–a3), the AZ31B alloy has experienced severe corrosion during the immersion. With immersion for 7 days, the initially smooth surface becomes rough with large corrosion cracks due to stress release from the natural passivation film. After immersion for 28 days, the size of the cracks increases. After immersion for 56 days, the surface delaminates from the substrate and is covered by the corrosion products. Enlarged SEM images reveal the presence of typical Ca-P particle deposits on the surface, which is attributed to the corrosion reaction involving calcium ions and phosphate ions in the SBF solution [45,46]. Zn-0 shows no significant changes in the non-porous area after immersion for 7 days but almost all the pores are connected by cracks. After 28 days, the pores are almost filled and the surface becomes rough accompanied by generation of cracks. After immersion for 56 days, the surface is occupied by corrosion products. Meanwhile, cracks with a size smaller than that of the AZ31B alloy emerge, indicating that corrosion damage is reduced (Fig. 8(b1–b3)). This is because the activity of MgO is lower than that of Mg, thereby resulting in slower corrosion. Comparatively, the zinc phosphate-doped MAO coatings demonstrate obvious alleviated corrosion morphology after different time immersions. After immersion for 7 days, there are almost no changes for Zn-1, Zn-2, and Zn-3 and the porous structure is maintained after 28 days (Fig. 8(c1, c2, d1, d2, e1, e2)). After immersion for 56 days, the surfaces of Zn-1 and Zn-2 show corrosion products. However, Zn-3 shows fewer corrosion products and maintains the original porous structure (Fig. 8(c3, d3, e3)).

EDS performed after immersion for 56 days reveals the presence of C, O, F, Mg, Al, Si, P, Cl, Ca, and Zn (Figs. 8 and S5–S9, and Table S7). C, Si, Cl, and Ca are introduced from the SBF solution, while Mg and Zn are introduced from the corrosion products $MgCl_2$, $Mg(OH)_2$, and $Zn(OH)_2$. In particular, recent research demonstrates that the formation of Zn $(OH)_2$ helps to handicap the infiltration corrosion by sealing the pores [29]. For the MAO coatings without zinc phosphate, when pitting occurs at the interface of the coating/alloy, the degradation of substrate will produce corrosion products along the interface, which increases interface stress and results in the coating peeling. In comparison, the MAO-doped coating with zinc phosphate would form the $Zn(OH)_2$ simultaneously with pitting, which could seal the infiltration channel partly and thereby restrain the amplification of pitting. Therefore, the MAO coating with zinc phosphate exhibits better corro-

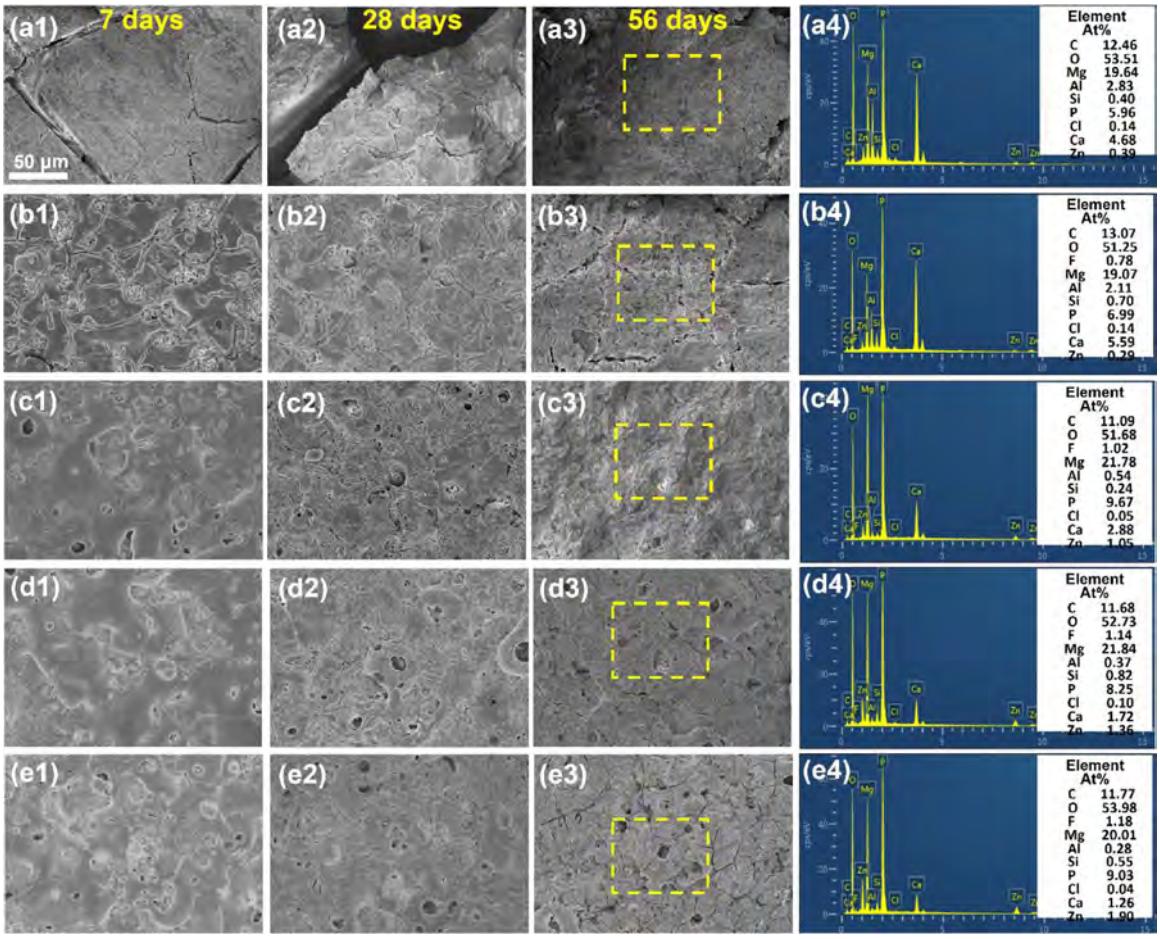

Fig. 8. SEM images and EDS spectra of the different specimens after immersion in SBF for 56 days: (a) AZ31B, (b) Zn-0, (c) Zn-1, (d) Zn-2, and (e) Zn-3.

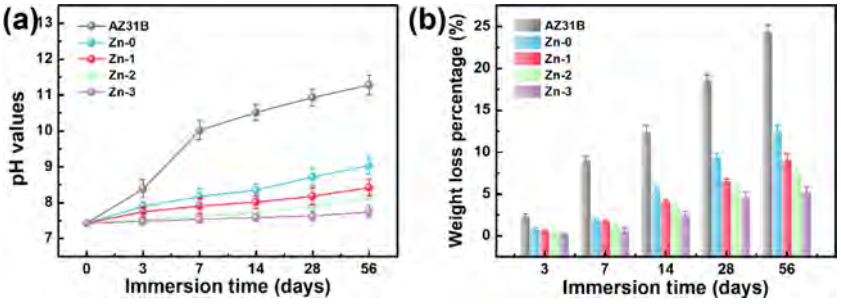

Fig. 9. (a) pH values of the SBF solution and (b) weight loss of the AZ31B alloy and MAO coatings doped with different concentrations of zinc phosphate during immersion in SBF.

sion resistance. The subsequent weight loss rate and pH changes in Fig. 9 also verify this deduction. The existence of Ca and P suggests that the production of hydroxyapatite-like precipitates can promote the growth of bone cells [47,48]. After the MAO treatment and zinc phosphate doping, the concentration of Ca element on the surface decreases after immersion. Because of the improvement in the corrosion resistance, the alkalinity decreases after immersion, and there is a decrease in the amount of hydroxyapatite containing Ca and P. These results indicate that doping with zinc phosphate regulates the degradation rate in SBF and alleviates the rapid degradation of the Mg alloy.

Fig. S10 displays SEM images of the cross-sections of the coatings after immersion for 56 days. The results reveal that the Zn-0 coating exhibits the most severe pitting corrosion at the interface with the substrate, showing chain-like pits. With increasing the doping content of zinc phosphate, the corrosion at the coating/substrate interface is alleviated. The Zn-3 coating only shows slight pitting pits at the interface, which implies that the corrosion resistance of the coating is improved due to zinc phosphate doping.

To analyze the degradation behavior, the pH value of the SBF solution and weight loss rate of the AZ31B alloy and MAO coatings doped with zinc phosphate are determined. The SBF solution shows that the pH values increase with immersion time, as shown in Fig. 9(a). For the AZ31B alloy, the pH reaches 8.39 and 10.02 after immersion for 3 and 7 days, respectively. Such high increasing rate should be ascribed to the rapid degradation which leads to the mass release of OH^- ions. As the corrosion reaction continues, the surface of the Mg alloy is gradually covered by the corrosion products, which decreases the corrosion rate and restrains

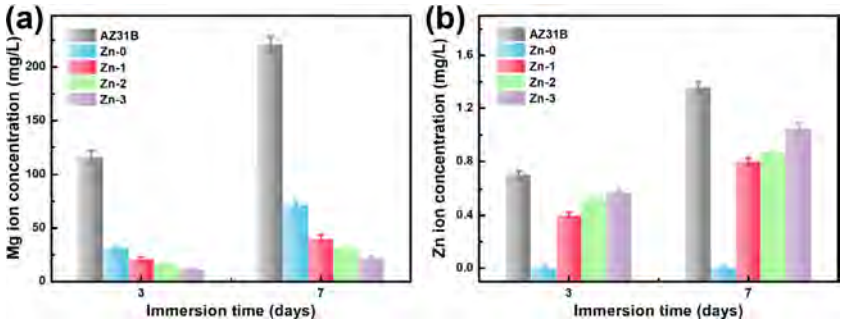

Fig. 10. Ion concentrations released from the AZ31B alloy and MAO coatings with different concentrations of zinc phosphate after immersion in SBF for 3 and 7 days: (a) Mg^{2+} and (b) Zn^{2+}.

the release of OH^-. Subsequently, the pH increases gradually and reaches a maximum of 11.28 after immersion for 56 days. Differently, the pH values of SBF solution immersed with MAO coatings demonstrate a slow-increasing tendency. With regard to Zn-0, the pH reaches 8.17 after immersion for 7 days and increases to 9.03 after 56 days, indicating an inhibited release of OH^-. After doping with zinc phosphate, the increase rate of the pH value slows initially and then goes up slightly. After 56 days, the maximum pH values are 8.42, 8.17, and 7.74 for Zn-1, Zn-2, and Zn-3, respectively, indicating better corrosion resistance for higher dopant concentrations.

Fig. 9(b) shows that the weight losses of specimens increase gradually during immersion. The AZ31B alloy shows the largest weight losses of 2.3%, 8.97%, 12.36%, 18.59%, and 24.37% after immersion for 3, 7, 14, 28, and 56 days, respectively. On the other hand, the AZ31B alloy coated with MAO coatings shows smaller weight loss. Especially for the MAO coating with zinc phosphate addition, they demonstrate the larger the zinc phosphate concentration, the smaller the weight loss. After immersion for 7 days, the weight loss rates of Zn-0, Zn-1, Zn-2, and Zn-3 are 1.84%, 1.66%, 1.29%, and 0.63%, respectively and after immersion for 56 days, they are 12.54%, 8.98%, 7.53%, and 5.22%, respectively.

Generally, the released ions affect cell growth in the physiological environment. Fig. 10 shows the Mg^{2+} and Zn^{2+} concentrations from the AZ31B alloy and AZ31B alloy coated with MAO coatings after immersion for 3 and 7 days. After immersion for 3 days, the Mg^{2+} concentration from the AZ31B alloy is 115.9 mg L^{-1}, while those from Zn-0, Zn-1, Zn-2, and Zn-3 are 31.0, 20.8, 16.7, and 10.6 mg L^{-1}, respectively (Fig. 10(a)). After immersion for 7 days, the Mg^{2+} concentrations increase. The AZ31B alloy shows the highest Mg^{2+} concentration of 221.1 mg L^{-1}, while those from Zn-0, Zn-1, Zn-2, and Zn-3 are 71.7, 40.1, 31.4, and 21.3 mg L^{-1}, respectively. Owing to the high activity, the AZ31B alloy corrodes quickly, creating an alkaline environment that is unfavorable for cell growth. The MAO coatings are mainly composed of inert MgO which cooperates with the sealing effect of zinc phosphate to decrease the degradation rate further. Therefore, the MAO coatings exhibit much lower Mg^{2+} ion-releasing rate.

Fig. 10(b) shows the variation of Zn^{2+} concentration of SBF solution immersed with different specimens. After immersion for 3 days, the Zn^{2+} concentration from AZ31B alloy is 0.71 mg L^{-1}, which is less than the released Mg^{2+} concentration because a small amount of Zn exists in the AZ31B alloy. Meanwhile, compared to the electrode potential of Mg, Zn is more negative and results in less dissolution. Differently, there is no Zn^{2+} release from Zn-0 as there is no zinc in the MAO coating. The Zn^{2+} concentrations released from Zn-1, Zn-2, and Zn-3 are 0.40, 0.52, and 0.57 mg L^{-1}, respectively, indicating that a small amount of zinc phosphate is dissolved. After immersion for 7 days, the Zn^{2+} concentrations released from the AZ31B alloy, Zn-1, Zn-2, and Zn-3 increase to 1.36, 0.80, 0.87, and 1.05 mg L^{-1}, respectively, while Zn-0 specimen still shows no release of Zn^{2+}. With increasing concentration of zinc phosphate, more Zn^{2+} ions are released from the AZ31B alloy coated with MAO coatings.

3.4. In vitro biological properties

Due to the excellent protective effect of the MAO coatings, the biological properties are determined. Fig. 11 shows the morphological changes of MC3T3-E1 osteoblasts on the specimens after culturing for 1, 3, and 7 days. The control Ti6Al4V surface after 1 day shows that the MC3T3-E1 osteoblasts are in a good spreading state with spindle-shaped cells evenly distributed on the surface. However, on the surface of the AZ31B alloy, only sporadic cell nuclei or cytoskeletons could be observed indicating the low cell viability. On the MAO coatings, there are more osteoblasts but spreading is poor. Especially the osteoblasts on Zn-0, some of them become shrinking. With the addition and increase of zinc phosphate concentration, the morphology of osteoblasts improves. After 3 days of culturing, the osteoblasts exhibit an obvious proliferation tendency. The osteoblasts on the control Ti6Al4V surface overlap and cover the entire surface. However, on the surface of the AZ31B alloy, only sporadic osteoblasts can be observed and the cells exhibit an elongated spindle shape. Comparatively, the osteoblasts on Zn-0 increase a little and have better morphology. With the addition of zinc phosphate, the Zn-1, Zn-2, and Zn-3 exhibit better cytocompatibility with significant enhanced proliferation of osteoblasts. After 7 days of culturing, the growth trend of osteoblasts varies among different specimens. On the control Ti6Al4V alloy, the osteoblasts show a high-density overlapping state after rapid proliferation and differentiation. On the other hand, there are only a small number of osteoblasts adhering to the AZ31B alloy with wrinkled shape showing poor vitality. The number of osteoblasts on Zn-0 decreases and most cells exhibit elongated and spindle shape. In contrast, the osteoblasts on the MAO coatings doped with zinc phosphate show dense coverage similar to that on the Ti6Al4V alloy indicating their excellent cytocompatibility.

Fig. S11 shows the results of the cytotoxicity tests of the control Ti6Al4V alloy, AZ31B alloy, and AZ31B alloy coated with MAO coatings. The AZ31B alloy shows obvious toxicity due to rapid degradation, while the other specimens meet the toxicity requirements for implantable medical materials (ISO10993–5). Fig. 12(a) shows the expression of LDH of BMSC after culturing on different specimens for different time. After culturing for 1 day, the LDH expression of BMSC cultured on the control Ti6Al4V alloy is the highest, whereas that on the AZ31B alloy is the lowest. After 3 days, the LDH expressions of BMSC cultured on all specimens increase. Comparatively, the LDH expression of BMSC cultured on the control Ti6Al4V alloy increases the most, while that on the AZ31B alloy is the lowest. For the MAO coatings, the LDH expression of BMSC cultured on

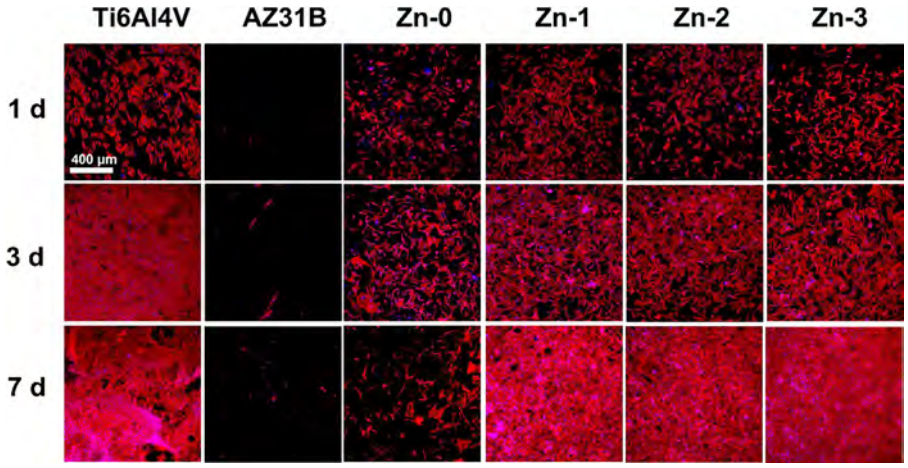

Fig. 11. Morphology of the MC3T3-E1 mouse osteoblasts cultured on the control Ti6Al4V alloy, AZ31B alloy, and MAO coatings doped with zinc phosphate for 1, 3, and 7 days. (Red represents the cell skeleton and blue represents the cell nuclei).

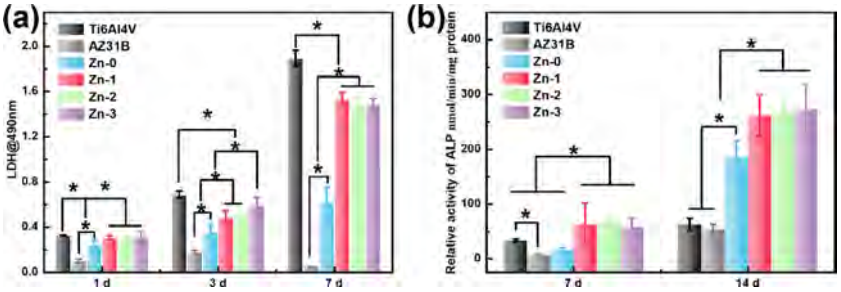

Fig. 12. (a) LDH and (b) ALP values of the BMSC cells cultured on the control Ti6Al4V alloy, AZ31B alloy, and MAO coatings doped with zinc phosphate.

them increases diversely and that on Zn-3 is higher than others. After 7 days, the LDH expressions of BMSC cultured on the control Ti6Al4V alloy and MAO coatings with zinc phosphate addition demonstrate a significant rising trend. On the contrary, the LDH expressions of BMSC cultured on the AZ31B alloy decrease obviously and the value is even lower than that with 1-day culturing. These comparative results indicate that the MAO coatings doped with zinc phosphate have better interface, which would benefit the proliferation and differentiation of osteoblasts. Fig. 12(b) shows the expressions of ALP of the BMSC cultured on different specimens demonstrating their corresponding mineralization ability. After 7 days of culturing, the ALP expressions of the BMSC cultured on MAO coatings doped with zinc phosphate are significantly higher than that of the control Ti6Al4V alloy. After 14 days of culturing, the ALP expression of the BMSC cultured on MAO coatings is more than twice that of the control Ti6Al4V alloy, especially the ones doped with zinc phosphate.

Since the LDH results reveal a consistent trend, it can be deduced that significant inhibition of ion release could improve the adhesion and growth of osteoblasts. The MAO coating with porous and rough surface is conducive to cell adhesion and proliferation, further improving its cytocompatibility. The well-improved corrosion resistance and surface morphology contribute to the tissue healing and maintaining of mechanical integrity in the early stage.

3.5. Tribological properties

As is well known, one major issue of MAO coatings is pitting corrosion along the coating/alloy interface. When the corrosive medium infiltrates and contacts the substrate, the rapid corrosion will generate massive hydrogen gas and loose corrosion products, which results in great interfacial stress and is prone to cause peeling failure [36]. Actually, the bone fixation implants have to face a certain degree of micromotion and wear, which can exacerbate the detachment of MAO coating and accelerate the pitting corrosion along the interface [37]. Therefore, reasonable wear resistance and self-sealing are important requirements for the MAO coating that could ensure its protecting effect on the implant. Fig. 13(a) shows the schematic diagram of the wear test for the AZ31B alloy and AZ31B alloy coated with MAO coatings with a load of 3 N for 3600 s, and the variation of the friction coefficients is shown in Fig. 13(b). Clearly, the friction coefficient of the AZ31B alloy greatly fluctuates around 0.30 with an amplitude of 0.15 for the whole test, but the friction coefficients of MAO coatings demonstrate a gradually increasing tendency with small fluctuation. Exactly, the friction coefficients of Zn-0 and Zn-1 almost gradually increase to the end obtaining the value of 0.74, while the friction coefficients of Zn-2 and Zn-3 gradually increase to 0.55. The difference is that the friction coefficient of Zn-2 reaches the maximum value at 2200s and then almost keeps unchanging. Such results indicate that the addition of zinc phosphate in MAO coating has an anti-friction effect [49–51]. Fig. 13(c) shows the wear track profiles of different specimens after friction for 3600 s. The wear on the AZ31B alloy is the highest manifested by wear track depth and width of 82 μm and 715 μm, respectively. However, the Zn-0, Zn-1, Zn-2, and Zn-3 have the wear depth of 25, 20, 13, and 10 μm, respectively, and their corresponding wear widths are 532, 408, 362, and 264 μm, respectively. The results are consistent with the trend of the friction coefficient, indicating that the zinc phosphate addition in MAO coatings reduces wear, which demonstrates that the higher the concentration of zinc phosphate, the less wear. Fig. 13(d) shows that the AZ31B alloy has the highest wear rate of 2.83×10^{-4} mm^3 N^{-1} m^{-1}, while the MAO coatings have decreased the wear rate gradually. The wear rate of Zn-0 is 6.52×10^{-5} mm^3

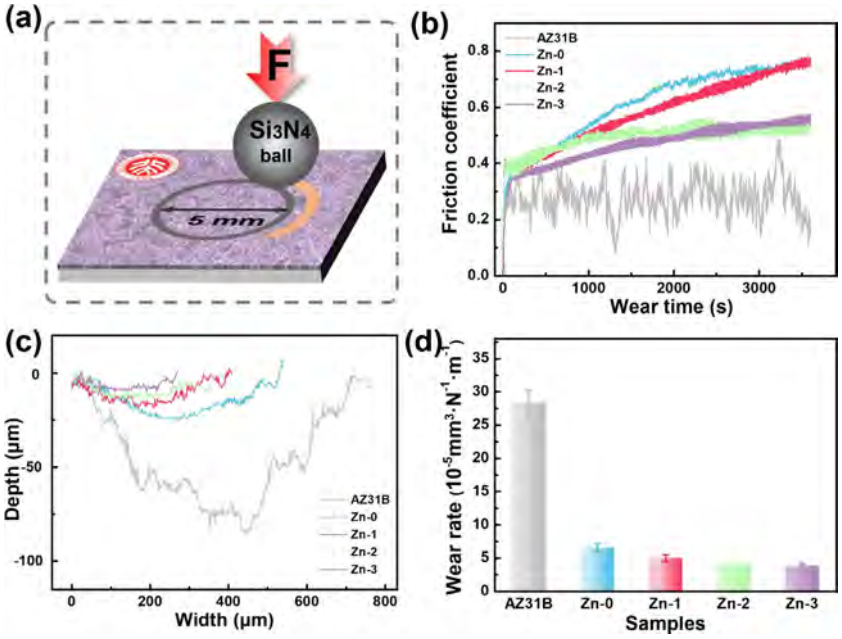

Fig. 13. Tribological properties of the AZ31B alloy and MAO coatings doped with zinc phosphate: (a) Schematic diagram of the friction process; (b) Friction coefficients; (c) Wear track profiles; (d) Wear rates.

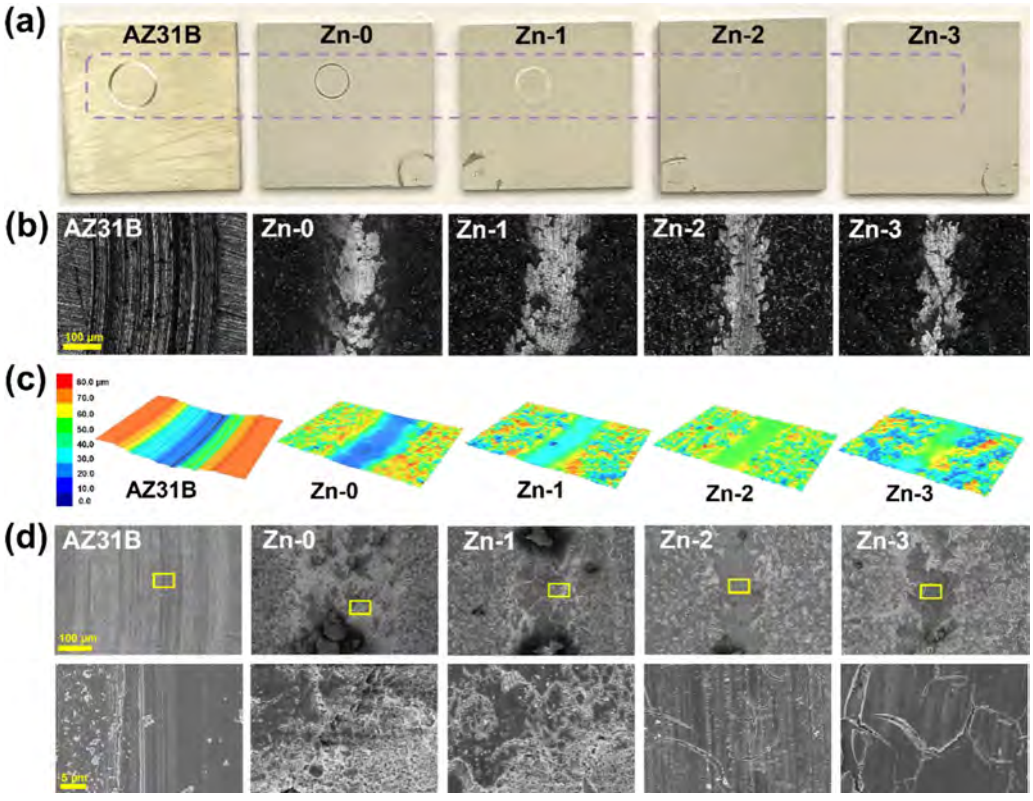

Fig. 14. Surface morphology of the AZ31B alloy and MAO coatings doped with zinc phosphate: (a) Optical images; (b) Planar LCSM images; (c) 3D LCSM images; (d) SEM micrographs.

N^{-1} m^{-1}, which is less than a quarter of the AZ31B alloy. After doping with zinc phosphate, the wear rates of MAO coatings decrease further and the values of Zn-1, Zn-2, and Zn-3 are 4.98×10^{-5}, 4.21×10^{-5}, and 3.81×10^{-5} mm^3 N^{-1} m^{-1}, respectively.

Fig. 14 shows the surface morphology of the specimens after the wear test. The optical observations show that the surface scratches become shallower after MAO and the scratch on Zn-3 is almost invisible (Fig. 14(a)). The features of scratches in both plane and three-dimensional modes observed by 3D laser confocal microscopy are shown in Fig. 14(b, c). The scratches on the AZ31B alloy are the widest and deepest, while the width and depth of the scratches on Zn-0, Zn-1, Zn-2, and Zn-3 are significantly reduced. The SEM observation on the worn surface of AZ31B alloy exhibits the typical furrow morphology with different depths, as shown in

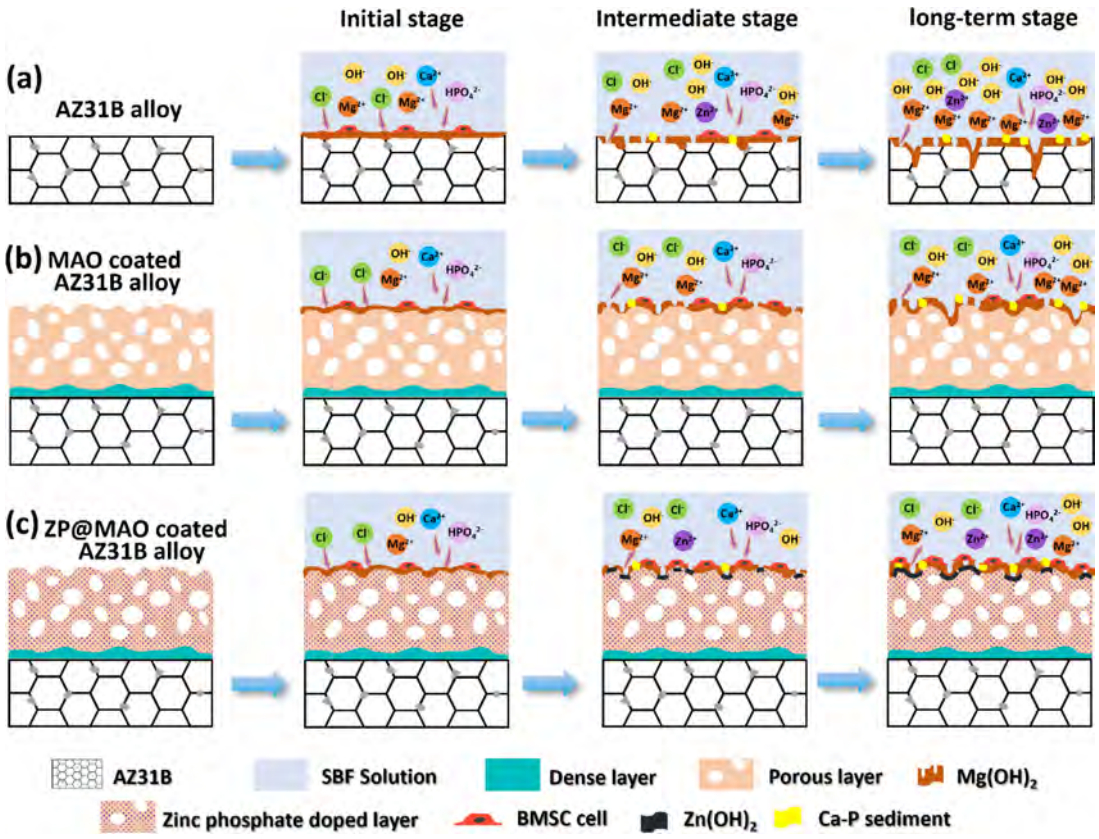

Fig. 15. Schematic diagram illustrating regulation of the degradation behavior and cytocompatibility for the MAO coatings and zinc phosphate addition: (a) AZ31B alloy; (b) MAO coating; (c) Zinc phosphate-doped MAO coating.

Fig. 14(d). The worn surfaces of Zn-0 and Zn-1 show some peeling and a large amount of debris. Such a phenomenon should be attributed to the three-dimensional porous structure whose protrusions are prone to be worn and peeled off by the hard grinding ball. Moreover, the main components of the MAO coating are MgO and $Mg_3(PO_4)_2$, which are easily crushed to increase the friction coefficient. In contrast, the worn surfaces of Zn-2 and Zn-3 are relatively flat and narrow with less debris indicating better wear resistance. Then, it can be concluded that the zinc phosphate addition improves the tribological properties of MAO coatings. In addition, when pitting occurs at the coating/substrate interface, the formation of $Zn(OH)_2$ could help to hinder penetration corrosion by sealing pores [29]. The synergistic effect of wear resistance and self-healing would effectively suppress coating detachment and failure caused by interface pitting corrosion, which enables the MAO coatings to meet the challenge of fretting wear and pitting corrosion simultaneously.

3.6. Influence of zinc phosphate on the degradation behavior and cytocompatibility

Based on the results, the AZ31B alloy with MAO coatings demonstrates better corrosion resistance and improved degradation behavior, which should be ascribed to the effectively regulated coating structure by zinc phosphate addition. According to the recent researches [29,35], Zn in the MAO coatings could promote the formation of $Zn(OH)_2$ and inhabit rapid infiltration corrosion. In the present research, the addition of zinc salt in electrolyte promotes the formation of zinc phosphate in MAO coating, which helps to form the inhibition layer and benefit the accumulation of Ca and P ions on the surface. The formed secondary protective layer decreases the degradation rate and contributes to regulating the micro-environment which cooperates with porous structure to obtain better cytocompatibility. The schematic diagram of the regulation effects of zinc phosphate on MAO coating is depicted in Fig. 15.

For the AZ31B alloy, the active Mg reacts with the SBF solution and generates $Mg(OH)_2$ forming a relatively loose layer on the surface during the initial stage of corrosion, which would alleviate the corrosion rate. The released Mg^{2+}, Zn^{2+}, and OH^- ions increase the pH of the SBF and the loose $Mg(OH)_2$ layer is gradually converted into water-soluble $MgCl_2$ by reacting with Cl^- forming corrosion pits. The Mg substrate is then re-exposed to SBF and undergoes the next process of rapid degradation. On account of the high density of crystal defects along grain boundaries, corrosion prefers to propagate along grain boundaries [52,53]. Therefore, during long-term degradation, conversion of $Mg(OH)_2$ becomes differentiated and the regions adjacent to grain boundaries corrode more significantly. The selective corrosion and degradation may result in the periodical corrosion rate and differentiated local corrosion, which destroys the structure integrality and releases more ions.

For the AZ31B alloy covered with MAO coating, the initial corrosion occurs mainly in the MgO-based MAO coating. Although MgO reacts with the SBF solution to form porous $Mg(OH)_2$ products, the reaction rate is so slow that ions release and pH increase only slightly. With the corrosion proceeding, the transformation of porous $Mg(OH)_2$ into water-soluble $MgCl_2$ exposes inner MgO in the MAO coating. After that, the reaction of MgO and transformation of $Mg(OH)_2$ repeat cyclically until the entire MAO coating is consumed. In addition, the Ca^{2+} and $PO4^{3-}$ ions in the SBF solution can also react during the corrosion process to form Ca-P particles, which deposit on the surface of the coating and enhance the density of the $Mg(OH)_2$ corrosion product film [45,46]. Therefore, the pH and ion release rate of the Zn-0 coating increase steadily

during corrosion but less than those of the AZ31B alloy. The addition of zinc phosphate in MAO coating changes the corrosion behavior by regulating the corrosion interface. In general, the reaction of MgO with SBF and the transformation of $Mg(OH)_2$ to $MgCl_2$ would occur normally in the zinc phosphate-doped MAO coating. However, zinc phosphate particles in the coating would participate in the initial reaction and form $Zn(OH)_2$ by releasing Zn^{2+}. As the $Zn(OH)_2$ product accumulates, a $Zn(OH)_2$ layer forms locally, which could inhibit the infiltration of the corrosion medium and decrease the corrosion rate [29,35,39,54]. Furthermore, the zinc phosphate particle prefers to accumulate adjacent to pores, which contributes to the sealing of pores by the reaction products. These regulations by zinc phosphate help to improve the porous MAO coatings significantly, because the infiltration through micropores is mitigated, enhancing the corrosion resistance.

By regulating the corrosion behavior of the Mg alloy, the degradation of mechanical properties can be controlled and the biocompatibility is improved simultaneously. As for the bare AZ31B alloy, the relative rapid degradation releases ions and increases pH in the micro-environment, leading to high alkaline and ion concentration, which is detrimental to cell viability. The MAO coating converts the AZ31B alloy surface into a porous structure which is beneficial to cell adhesion and proliferation [55]. In addition, the MAO coatings retards degradation and pH rising rate. Therefore, the cells on MAO coatings exhibit a better state in a short time. However, the released ions and pH still reach a high level after an intermediate-term immersion, resulting the low cell viability. The addition of zinc phosphate in MAO coating changes the intermediate and long-term corrosion degradation behavior by restraining rapid infiltration corrosion. The relatively weak alkaline micro-environment with an appropriate concentration of Mg^{2+} is beneficial to cell proliferation [56]. Moreover, zinc phosphate promotes the accumulation of Ca and P on the surface for better mineralization [57]. Zn^{2+} can also regulate osteogenesis by activating the Wnt/β-catenin signaling pathway. Even though cell proliferation on the zinc phosphate-doped MAO coatings is not the highest, the accumulated Ca and P accelerate mineralization leading to the highest ALP value. Therefore, the higher the zinc phosphate concentration, the better the corrosion behavior, wear, and cytocompatibility. However, superfluous zinc phosphate influences the MAO processing and coating structure. In summary, the appropriate addition of zinc phosphate in MAO coating can simultaneously optimize the key functions of Mg alloy such as corrosion resistance, wear resistance, and cell compatibility, avoiding the limitations of single functional MAO coatings. Therefore, it provides a potential method for the surface modification of biodegradable Mg alloy used as bone fixation implant.

4. Conclusion

To regulate the corrosion and degradation behavior of the AZ31B alloy for implantable bone fixation applications, the MAO coatings with different zinc phosphate additions were fabricated and evaluated under *in vitro* physiological conditions. The corrosion potential of the AZ31B alloy coated with MAO coatings increases with zinc phosphate concentration reaching a maximum of −1.427 V, and the corrosion current density decreases to 1.413×10^{-8} A cm^{-2}. The charge transfer resistance increases to 2.624×10^{5} ohm cm^2, indicating that the zinc phosphate-doped MAO coating has excellent corrosion resistance in SBF. Incorporation of the proper amount of zinc phosphate into the MAO coatings optimizes the degradation rate of Mg alloy, reduces the release rate of Mg^{2+} and OH^- generated by the corrosion reaction, and alleviates the generation of a large number of corrosion products. After immersion for 56 days, the weight loss decreases from 24.37% for the substrate to 5.22%. Zinc phosphate is converted into $Zn(OH)_2$ during immersion to restrain the infiltration corrosion and provide a weakly alkaline micro-environment for cell proliferation, differentiation, and mineralization giving rise to excellent cytocompatibility. In addition, zinc phosphate enhances the wear resistance of the AZ31B alloy coated with MAO coatings and obtains the minimum value of 3.81×10^{-5} mm^3 N^{-1} m^{-1}. The zinc phosphate-doped MAO coating optimizes the corrosion degradation behavior, cytocompatibility, and tribological properties, which provides a potential surface modification choice for Mg-based bone fixation implants.

Declaration of Competing Interest

The authors declare that they have no known competing financial interests or personal relationships that could have appeared to influence the work reported in this paper.

Acknowledgments

This work is financially supported by the Shenzhen-Hong Kong Research and Development Fund (No. SGDX20201103095406024), the 2022 Shenzhen Sustainable Supporting Funds for Colleges and Universities (No. 20220810143642004), the Shenzhen Basic Research Project (Nos. JCYJ20200109144608205 and JCYJ20210324120001003), the Guangdong Basic and Applied Basic Research Foundation (Nos. 2020A1515011301 and 2021A1515012246), the Peking University Shenzhen Graduate School Research Start-up Fund of Introducing Talent (No. 1270110273), the Shenzhen Postdoctoral Research Fund Project after Outbound (No. 2129933651), the China Postdoctoral Science Foundation (No. 2023M730032), the City University of Hong Kong Strategic Research Grants (SRG) (7005505), the City University of Hong Kong Donation Research Grants (No. 9220061 and DON-RMG No. 9229021), the Guangdong-Hong Kong Technology Cooperation Funding Scheme (TCFS) (No. GHP/085/18SZ), the Shenzhen-Hong Kong Technology Cooperation Funding Scheme (TCFS) (No. GHP/149/20SZ and CityU 9440296), and the IER Foundation (Nos. IERF2020001 and IERF202102).

Supplementary materials

Supplementary material associated with this article can be found, in the online version, at doi:10.1016/j.jmst.2023.09.019.

References

[1] D. Cai, X. Zhao, L. Yang, R. Wang, G. Qin, D. Chen, E. Zhang, J. Mater. Sci. Technol. 81 (2021) 13–25.
[2] K.M. Sanders, G.C. Nicholson, A.M. Ugoni, E. Seeman, J.A. Pasco, M.A. Kotowicz, J. Epidemiol, Commun. Health 56 (2002) 466–470.
[3] M.P. Staiger, A.M. Pietak, J. Huadmai, G. Dias, Biomaterials 27 (2006) 1728–1734.
[4] Z.M. Shi, M. Liu, A. Atrens, Corros. Sci. 52 (2010) 579–588.
[5] Z.Z. Yin, W.C. Qi, R.C. Zeng, X.B. Chen, C.D. Gu, S.G. Guan, Y.F. Zheng, J. Magnes. Alloy. 8 (2020) 42–65.
[6] J.F. Song, J. Chen, X.M. Xiong, X.D. Peng, D.L. Chen, F.S. Pan, J. Magnes. Alloy. 10 (2022) 863–898.
[7] Y. Xin, T. Hu, P.K. Chu, Acta Biomater. 7 (2011) 1452–1459.
[8] Z.Y. Ding, L.Y. Cui, R.C. Zeng, Y.B. Zhao, S.K. Guan, D.K. Xu, C.G. Lin, J. Mater. Sci. Technol. 34 (2018) 1550–1557.
[9] R.W. Li, N.T. Kirkland, J. Truong, J. Wang, P.N. Smith, N. Birbilis, D.R. Nisbet, J. Biomed. Mater. Res. A 102 (2014) 4346–4357.
[10] T. Liang, L.L. Zeng, Y.Z. Shi, H.B. Pan, P.K. Chu, K.W.K. Yeung, Y. Zhao, Bioact. Mater. 6 (2021) 3049–3061.
[11] X.B. Chen, D.R. Nisbet, R.W. Li, P.N. Smith, T.B. Abbott, M.A. Easton, D.H. Zhang, N. Birbilis, Acta Biomater 10 (2014) 1463–1474.
[12] Y.F. Zheng, X.N. Gu, F. Witte, Mater. Sci. Eng. R 77 (2014) 1–34.
[13] Y. Kang, B. Du, Y. Li, B. Wang, L. Sheng, L. Shao, Y. Zheng, T. Xi, J. Mater. Sci. Technol. 35 (2019) 6–18.
[14] J. Wang, L. Meng, Z. Zhang, B. Sa, X. Fu, L. Sheng, D. Xu, Y. Zheng, J. Magnes. Alloy. 11 (2023) 1074–1082.
[15] N. Zhang, W. Wang, X. Zhang, K.C. Nune, Y. Zhao, N. Liu, R.D.K. Misra, K. Yang, L. Tan, J. Yan, Bioact. Mater. 6 (2021) 1765–1776.

[16] R.C. Zeng, W. Dietzel, F. Witte, N. Hort, C. Blawert, Adv. Eng. Mater. 10 (2008) 3–14.
[17] F. Witte, Acta Biomater. 6 (2010) 1680–1692.
[18] F. Witte, V. Kaese, H. Haferkamp, E. Switzer, A. Meyer-Lindenberg, C.J. Wirth, H. Windhagen, Biomaterials 26 (2005) 3557–3563.
[19] M. Daavari, M. Atapour, M. Mohedano, H.M. Sánchez, J. Rodríguez-Hernández, E. Matykina, R. Arrabal, A. Taherizadeh, J. Magnes. Alloy. 10 (2022) 3217–3233.
[20] C. Yu, L.Y. Cui, Y.F. Zhou, Z.Z. Han, X.B. Chen, R.C. Zeng, Y.H. Zou, S.Q. Li, F. Zhang, E.H. Han, S.K. Guan, Surf. Coat. Technol. 344 (2018) 1–11.
[21] J.F. Chen, W.X. Lin, S.Y. Liang, L.C. Zou, C. Wang, B.S. Wang, M.F. Yan, X.P. Cui, Appl. Surf. Sci. 463 (2019) 535–544.
[22] A. Fattah-alhosseini, R. Chaharmahali, K. Babaei, J. Magnes. Alloy. 8 (2020) 799–818.
[23] A. Fattah-alhosseini, R. Chaharmahali, K. Babaei, M. Nouri, M.K. Keshavarz, M. Kaseem, J. Magnes. Alloy. 10 (2022) 2354–2383.
[24] S.F. Fischerauer, T. Kraus, X. Wu, S. Tangl, E. Sorantin, A.C. Hanzi, J.F. Loffler, P.J. Uggowitzer, A.M. Weinberg, Acta Biomater. 9 (2013) 5511–5420.
[25] D. Veys-Renaux, C.E. Barchiche, E. Rocca, Surf. Coat. Technol. 251 (2014) 232–238.
[26] M. Sun, A. Yerokhin, M.Y. Bychkova, D.V. Shtansky, E.A. Levashov, A. Matthews, Corros. Sci. 111 (2016) 753–769.
[27] B. Mingo, Y. Guo, A. Nemcov, A. Gholinia, M. Mohedano, M. Sun, A. Matthews, A. Yerokhin, Electrochim. Acta 299 (2019) 772–788.
[28] Y. Gao, L.F. Zhao, X.H. Yao, R.Q. Hang, X.Y. Zhang, B. Tan, Surf. Coat. Technol. 349 (2018) 434–441.
[29] C. Yang, J. Huang, S.H. Cui, R.Y.K. Fu, L.Y. Sheng, D.K. Xu, X.B. Tian, Y.F. Zheng, P.K. Chu, Z.Z. Wu, J. Magnes. Alloy. (2023), doi:10.1016/j.jma.2023.02.008.
[30] M. Roknian, A. Fattah-alhosseini, S.O. Gashti, M.K. Keshavarz, J. Alloy. Compd. 740 (2018) 330–345.
[31] F. Iqbal, A. Ali, M. Naveed, F. Ikram, H. Fatima, Surf. Coat. Technol. 457 (2023) 129301.
[32] L. Xu, E. Zhang, K. Yang, J. Mater. Sci. 20 (2008) 859–867.
[33] E.L. Zhang, W.W. He, H. Du, K. Yang, Mater. Sci. Eng. A 488 (2008) 102–111.
[34] Y.P. Liu, X. Cheng, X.Y. Wang, Q. Sun, C.X. Wang, P. Di, Y. Lin, Mater. Sci. Eng. C 131 (2021) 112491.
[35] C. Yang, H. Cai, S.H. Cui, J. Huang, J.Y. Zhu, Z.C. Wu, Z.Y. Ma, R.K.Y. Fu, L.Y. Sheng, X.B. Tian, P.K. Chu, Z.Z. Wu, Surf. Coat. Technol. 433 (2022) 128148.
[36] Z.Y. Ding, L.Y. Cui, X.B. Chen, R.C. Zeng, S.K. Guan, S.Q. Li, F. Zhang, Y.H. Zou, Q.Y. Liu, J. Alloy. Compd. 764 (2018) 250–260.
[37] J.X. Chen, Y. Yang, I.P. Etim, L.L. Tan, K. Yang, R.D.K. Misra, J.H. Wang, X.P. Su, Trans. Nonferrous Met. Soc. China 33 (2023) 1411–1424.
[38] F. Jamali-Sheini, K.R. Patil, Appl. Surf. Sci. 257 (2011) 8366–8372.
[39] Q. Huang, L.L. Liu, Z.Z. Wu, S. Ji, H. Wu, P.H. Chen, Z.Y. Ma, Z.C. Wu, R.K.Y. Fu, H. Lin, X.B. Tian, F. Pan, P.K. Chu, Surf. Coat. Technol. 384 (2020) 125321.
[40] J. 'Swiatowska, V. Lair, C. Pereira-Nabais, G. Cote, P. Marcus, A. Chagnes, Appl. Surf. Sci. 257 (2011) 9110–9119.
[41] N.V. Phuong, M. Gupta, S. Moon, Trans. Nonferrous Metals Soc. China 27 (2017) 1087–1095.
[42] L. Pezzato, R. Babbolin, P. Cerchier, M. Marigo, P. Dolcet, M. Dabal'a, K. Brunelli, Corros. Sci. 173 (2020) 108741.
[43] S.V. Gnedenkov, S.L. Sinebryukhov, V.I. Sergienko, Russ. J. Electrochem. 42 (2006) 197–211.
[44] A. Jangde, S. Kumar, C. Blawert, Corros. Sci. 157 (2019) 220–246.
[45] A.M. Zhang, P. Lenin, R.C. Zeng, M.B. Kannan, J. Magnes. Alloy. 10 (2022) 1154–1170.
[46] B. Du, Z. Hu, J. Wang, L. Sheng, H. Zhao, Y. Zheng, T. Xi, Bioact. Mater. 5 (2020) 219–227.
[47] M. Rahman, Y.C. Li, C.E. Wen, J. Magnes. Alloy. 8 (2020) 929–943.
[48] J.A. Li, L. Chen, X.Q. Zhang, S.K. Guan, Mater. Sci. Eng. C 109 (2020) 110607.
[49] J.P. Bricout, P. Hivart, J. Oudin, Y. Ravalard, J. Mater, Process. Technol. 24 (1990) 3–12.
[50] P. Hivart, J.P. Bricout, J. Oudin, J.Y. Dauphin, J. Tribol.-Trans. ASME 114 (1992) 248–249.
[51] A. Dubois, L. Dubar, P. Picart, J. Oudin, J. Mater. Eng. Perform. 56 (1996) 734–742.
[52] B.J. Wang, D.K. Xu, X. Cai, Y.X. Qiao. L.Y. Sheng, J. Magnes. Alloy. 9 (2021) 560–568.
[53] B.N. Du, Z.Y. Hu, L.Y. Sheng, D.K. Xu, Y.X. Qiao, B.J. Wang, J. Wang, Y.F. Zheng, T.F. Xi, J. Mater. Sci. Technol. 60 (2021) 44–55.
[54] J. Wang, L.Z. Meng, W.X. Xie, C. Ji, R.H. Wang, P.H. Zhang, L.L. Jin, L.Y. Sheng, Y.F. Zheng, J. Magnes. Alloy. (2022), doi:10.1016/j.jma.2022.09.025.
[55] C. Wang, J. Wu, L.Y. Liu, D.L. Xu, Y.B. Liu, S.J. Li, W.T. H, J. Wang, X. Chen, L.Y. Sheng, Lin H.C, D.S. Yu, Front. Chem. 11 (2023) 1190630.
[56] J.L. Wang, J.K. Xu, X.L. Wang, L.Y. Sheng, L.Z. Zheng, B. Song, G. Wu, R. Zhang, H. Yao, N.Y. Zheng, M.T.Y. Ong, P.S.H. Yung, L. Qin, Biomaterials 268 (2021) 120576.
[57] C.L. Wen, J.M. Qian, L.J. Luo, J.H. Zeng, B.S. Sa, X. Zhan, J. Wang, L.Y. Sheng, Y.F. Zheng, J. Non-Cryst. Solids 578 (2022) 121329.

Supporting Information for

Optimization of the *in vitro* biodegradability, cytocompatibility, and wear resistance of the AZ31B alloy by micro-arc oxidation coatings doped with zinc phosphate

Chao Yang [a,g], Suihan Cui [a,b,*], Ricky Fu [b], Liyuan Sheng [c,d,*], Min Wen [c], Daokui Xu [e], Ying Zhao [f], Yufeng Zheng [c], Paul K. Chu [b], Zhongzhen Wu [a,*]

[a] School of Advanced Materials, Peking University Shenzhen Graduate School, Shenzhen 518055, China

[b] Department of Physics, Department of Materials Science & Engineering, and Department of Biomedical Engineering, City University of Hong Kong, Tat Chee Avenue, Kowloon, Hong Kong 999077, China

[c] Shenzhen Institute, Peking University, Shenzhen 518057, China

[d] PKU-HKUST Shenzhen – Hong Kong Institution, Shenzhen 518057, China

[e] Key Laboratory of Nuclear Materials and Safety Assessment, Institute of Metal Research, Chinese Academy of Sciences, Shenyang 110016, China

[f] Shenzhen Institutes of Advanced Technology, Chinese Academy of Sciences, Shenzhen 518055, China

[g] National Engineering Research Center of Light Alloy Net Forming and State Key Laboratory of Metal Matrix Composite, Shanghai Jiao Tong University, Shanghai 200240, China

∗ Corresponding authors.

E-mail addresses: lysheng@yeah.net (L.Y. Sheng); cuish@pku.edu.cn (S.H. Cui); wuzz@pkusz.edu.cn (Z.Z. Wu).

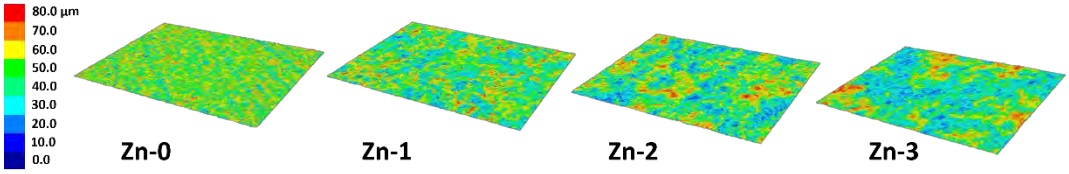

Fig. S1. Three-dimensional LCSM images of the MAO coatings doped with different amounts of zinc phosphate.

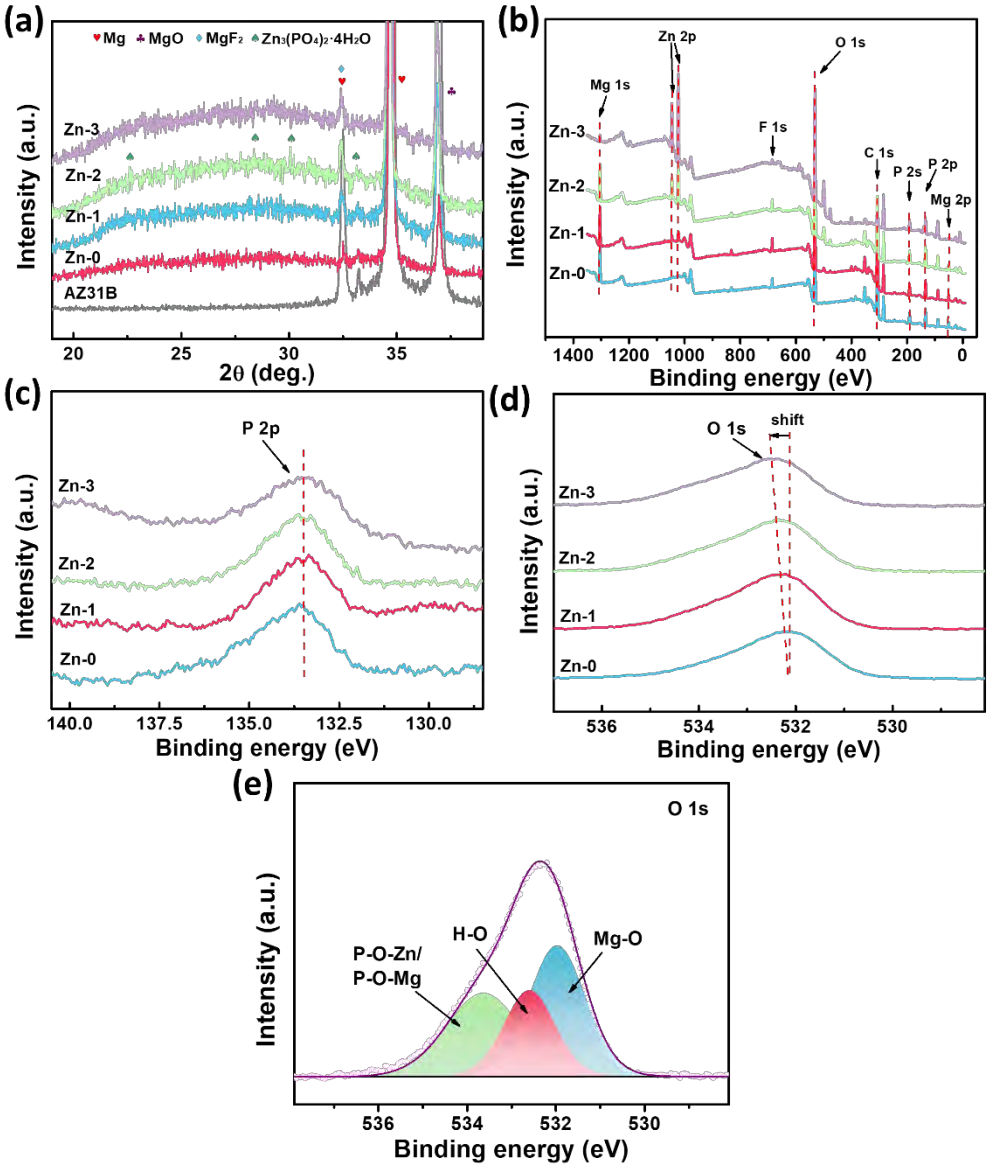

Fig. S2. (a) High magnification XRD spectra; XPS spectra: (b) Survey, (c) P 2p, and (d) O 1s; (e) Fitted O 1s spectrum of Zn-3.

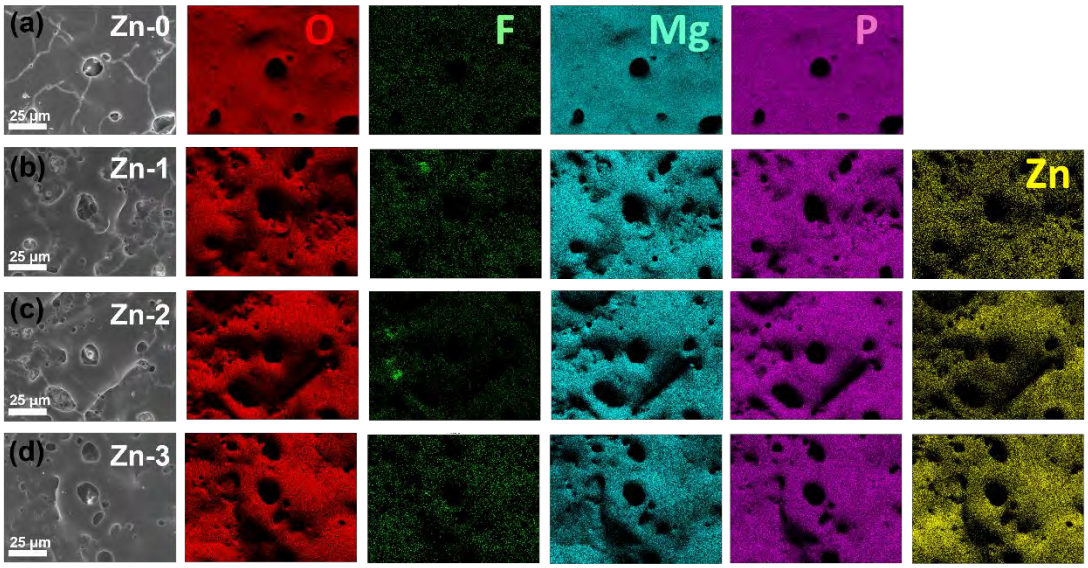

Fig. S3. SEM images and EDS elemental distributions of the MAO coatings with different zinc phosphate contents: (a) Zn-0, (b) Zn-1, (c) Zn-2, and (d) Zn-3.

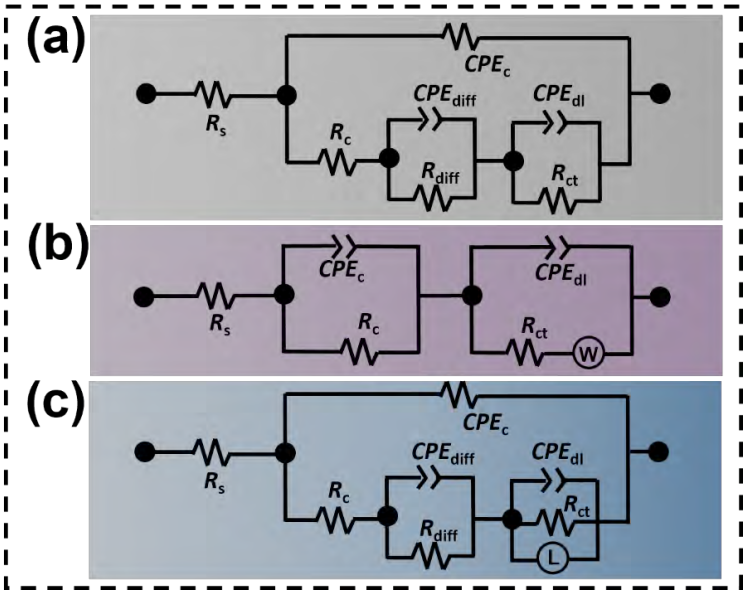

Fig. S4. Equivalent fitted circuits for the samples immersed in SBF: (a) R(Q(R(QR)(QR))), (b) R(RQ)(Q(RW)), and (c) R(Q(R(QR)(QRL))).

The results of AZ31B after immersion for 3 and 7 days are analyzed by the EC model in Fig. S4(a) and those after 14 and 28 days are analyzed by the EC model in Fig. S4(b). The results after immersion for 56 days are analyzed using the EC model in Fig. S4(c). The results of Zn-0 after immersion for 3, 7, 14, and 56 days are analyzed by the EC model in Fig. S4(a), while those after immersion for 28 days are analyzed by the EC model in Fig. S4(b). The results of Zn-1 after 3, 7, 14, and 56 days are analyzed by the EC model in Fig. S4(a) and those after 28 days are analyzed using the EC model in Fig. S4(b). The results of Zn-2 after 3, 7, 14, and 28 days are analyzed by the EC model in Fig. S4(a) and those after 56 days are analyzed by the EC model in Fig. S4(b). The results of Zn-3 after 3, 7, 14, 28, and 56 days are analyzed by the EC model shown in Fig. S4a.

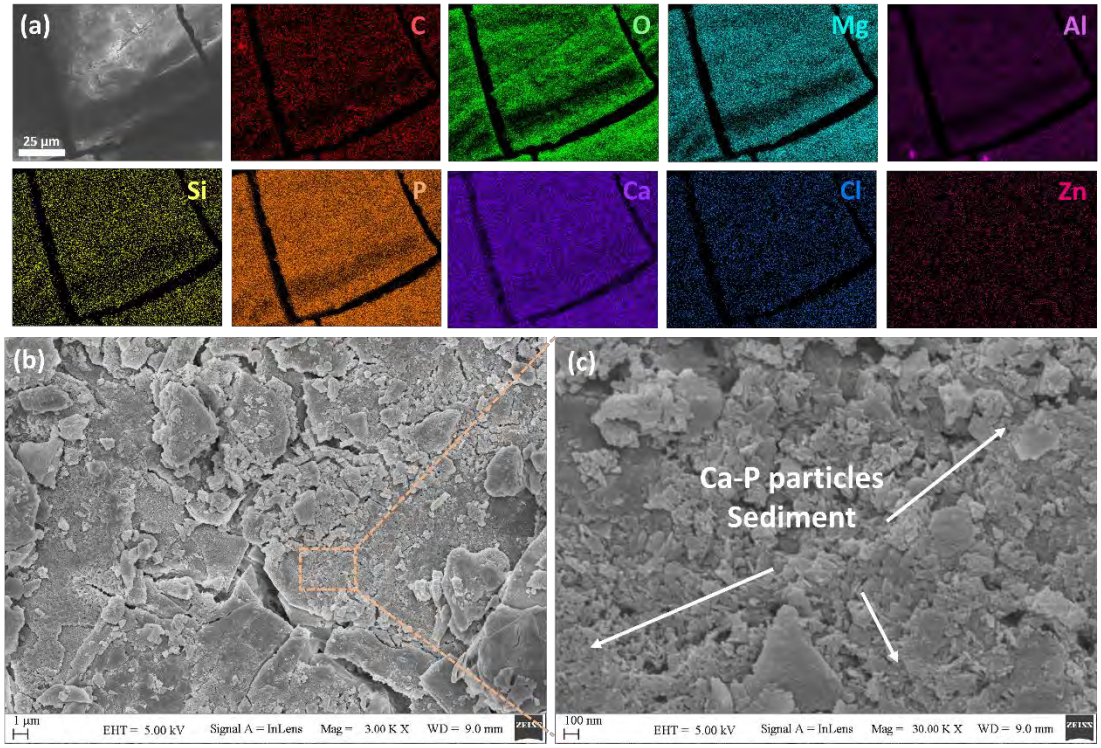

Fig. S5. (a) EDS elemental maps of the AZ31B alloy after immersion for 56 days; (b, c) High magnification surface corrosion morphology.

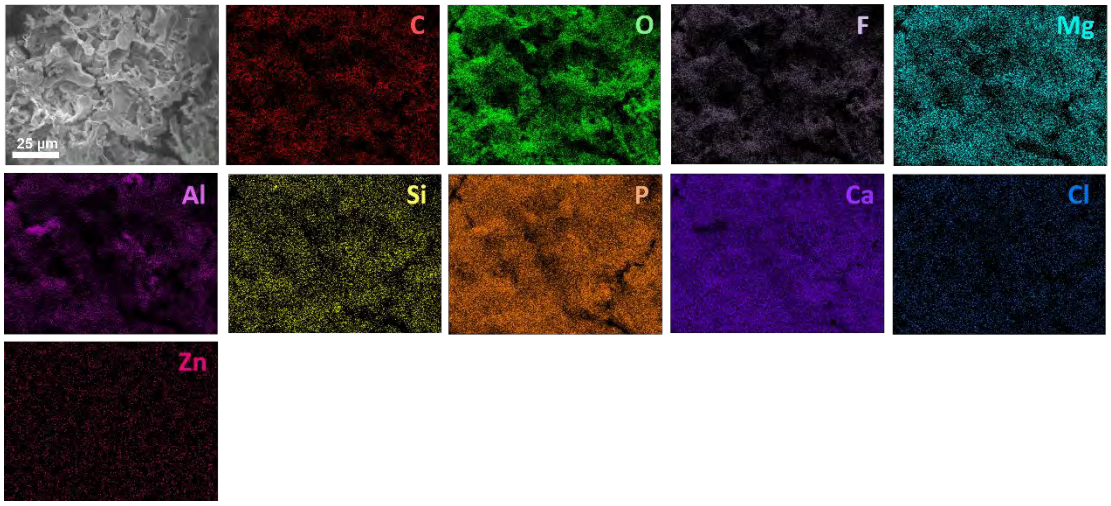

Fig. S6. EDS element maps of Zn-0 after immersion for 56 days.

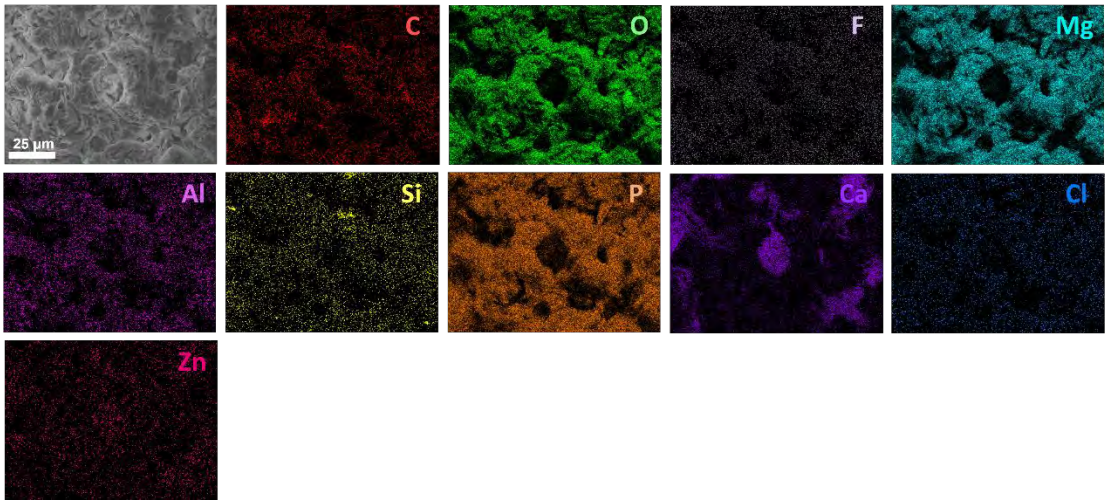

Fig. S7. EDS elemental maps of Zn-1 after immersion for 56 days.

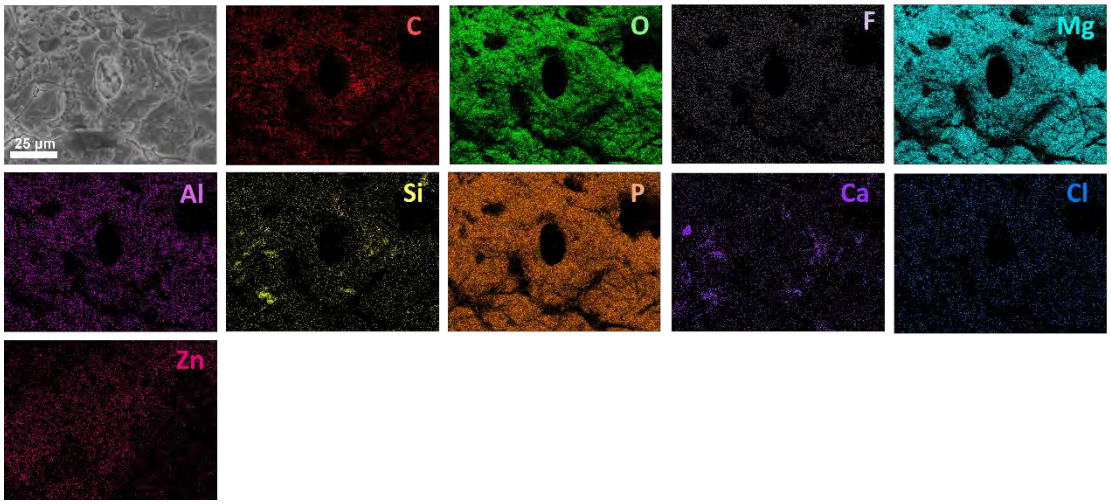

Fig. S8. EDS elemental maps of Zn-2 after immersion for 56 days.

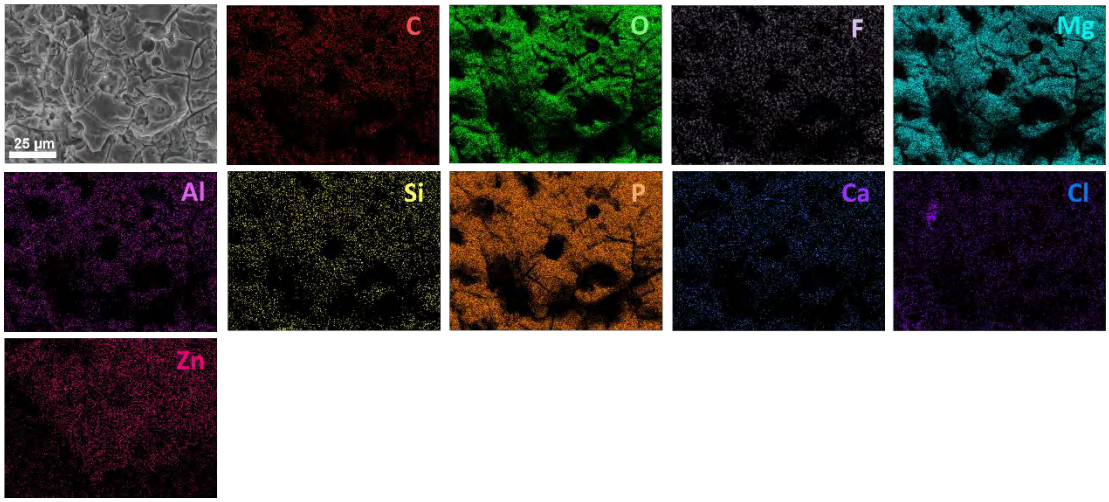

Fig. S9. EDS elemental maps of Zn-3 after immersion for 56 days.

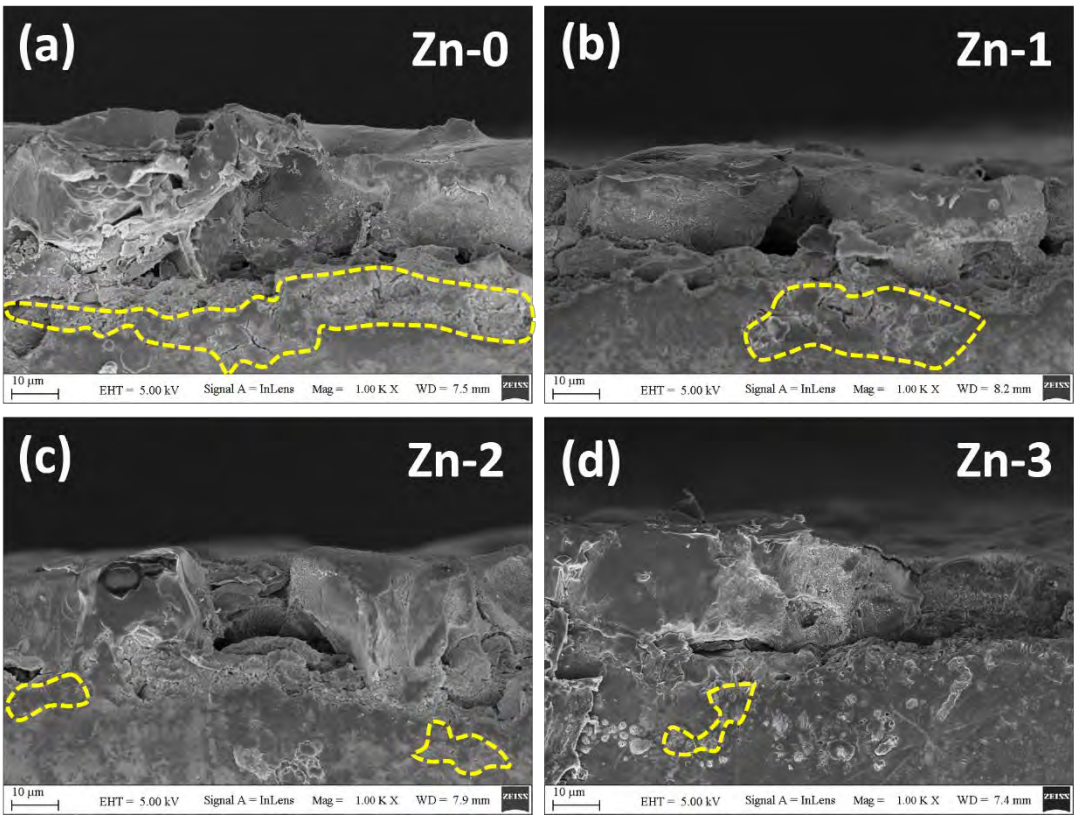

Fig. S10. SEM images of the cross-sections of the MAO coatings with different zinc phosphate contents after immersion for 56 days: (a) Zn-0, (b) Zn-1, (c) Zn-2, and (d) Zn-3.

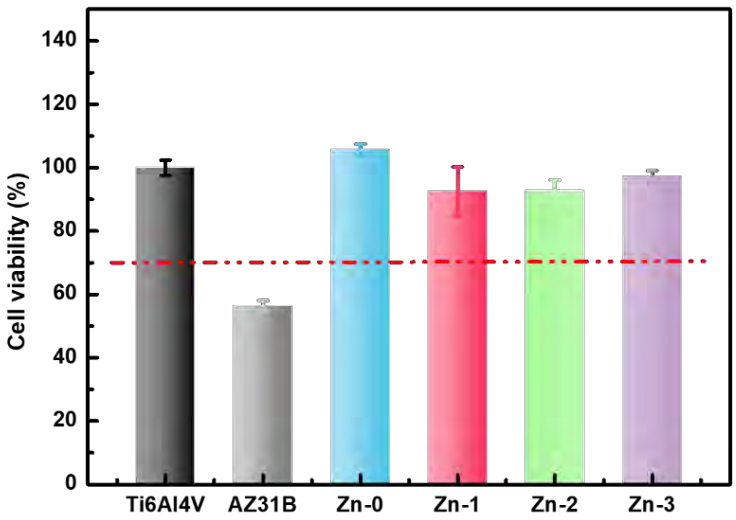

Fig. S11. Cytotoxicity of the control Ti6Al4V alloy, AZ31B alloy, and MAO coatings doped with different zinc phosphate concentrations.

To analyze the effects of the MAO coatings on the cytotoxicity of the AZ31B alloy, the cell viability of the Ti6Al4V alloy, AZ31B alloy, and zinc phosphate-doped MAO coatings is determined according to the ISO10993-5 standard. The bone marrow mesenchymal stem cells (BMSCs) exhibit different viabilities after culturing in the extraction solution for 3 days. Owing to the small ion release rate of the control Ti6Al4V alloy, the BMSCs show high activity but lower activity in the extracted solution of the AZ31B alloy, indicating that the higher concentration of ions produced by rapid corrosion increases the pH and weakens the cell activity. As for the MAO coating without zinc phosphate, the cell activity is higher than that of the control Ti6Al4V alloy due to the beneficial effects of a suitable amount of Mg^{2+} ions in the extracted solution on cell proliferation and differentiation. After incorporating

increasing concentrations of zinc phosphate into the MAO coating, the cell activity decreases slightly due to the release of Zn^{2+}. Overall, the AZ31B alloy samples protected by MAO coatings show excellent cell activity which exceeds the requirements of orthopedic implants and the biocompatibility is comparable to that of the control Ti6Al4V alloy.

Table S1. Thickness and surface roughness R_a of the MAO coatings.

Sample	Thickness (μm)	Surface roughness (μm)
Zn-0	41.5 ± 3.7	0.92 ± 0.19
Zn-5	44.1 ± 3.6	1.43 ± 0.37
Zn-10	45.4 ± 3.1	1.84 ± 0.46
Zn-15	47.3 ± 4.2	2.52 ± 0.35

Table S2. EIS fitting results of the AZ31B alloy immersed in the SBF solution for different time durations based on the EC.

Immersion time	3 day	7 day	14 day	28 day	56 day
CPE_c	4.749×10^{-5}	3.315×10^{-5}	1.481×10^{-8}	7.073×10^{-9}	2.938×10^{-7}
n_c	0.4176	0.2948	0.5451	0.8176	0.9436
R_c (ohm cm^2)	96.07	2.116×10^{2}	2.403×10^{4}	1.286×10^{5}	5.585×10^{3}
CPE_{diff}	1.162×10^{-5}	8.762×10^{-6}	–	–	2.499×10^{-6}
n_{diff}	0.7534	0.6665	–	–	0.7503
R_{diff} (ohm cm^2)	5.859×10^{2}	8.705×10^{2}	–	–	6.462×10^{4}
W (S sec^5 cm^{-2})	–	–	7.834×10^{-5}	8.856×10^{-7}	–
CPE_{dl}	4.509×10^{-4}	4.730×10^{-5}	2.552×10^{-7}	8.473×10^{-8}	6.493×10^{-5}
n_{dl}	0.7932	0.8975	0.7006	0.6685	0.4753
R_{ct} (ohm cm^2)	5.939×10^{2}	2.521×10^{3}	1.882×10^{5}	3.057×10^{5}	1.239×10^{3}
L (H cm^2)	–	–	–	–	5.680×10^{3}
R_l (ohm cm^2)	–	–	–	–	9.642×10^{3}

Table S3. EIS fitting results of the Zn-0 coating immersed in the SBF solution for different time durations based on the EC.

Immersion time	3 day	7 day	14 day	28 day	56 day
CPE_c	3.246×10^{-6}	2.287×10^{-6}	4.048×10^{-8}	1.666×10^{-8}	1.062×10^{-6}
n_c	0.8160	0.4729	0.7895	0.7172	0.3458
R_c (ohm cm^2)	8.481×10^{2}	1.271×10^{3}	1.461×10^{4}	4.653×10^{4}	2.582×10^{3}
CPE_{diff}	6.379×10^{-6}	2.568×10^{-6}	1.219×10^{-6}	–	1.092×10^{-5}
n_{diff}	0.8220	0.5089	0.3956	–	0.8927
R_{diff} (ohm cm^2)	3.191×10^{3}	1.764×10^{4}	4.963×10^{4}	_	1.957×10^{3}
W (S sec^5 cm^{-2})	–	–	–	2.098×10^{-6}	–
CPE_{dl}	1.115×10^{-4}	2.292×10^{-5}	7.066×10^{-7}	1.352×10^{-7}	2.755×10^{-5}
n_{dl}	0.5524	0.8453	0.8164	0.5051	0.7523
R_{ct} (ohm cm^2)	2.445×10^{3}	7.065×10^{3}	1.271×10^{5}	1.920×10^{5}	3.419×10^{3}

Table S4. EIS fitting results of the Zn-1 coating immersed in the SBF solution for different time durations based on the EC.

Immersion time	3 day	7 day	14 day	28 day	56 day
CPE_c	5.495×10^{-8}	2.685×10^{-7}	8.508×10^{-7}	4.160×10^{-8}	1.068×10^{-5}
n_c	0.7410	0.6178	0.6924	0.6970	0.8483
R_c (ohm cm^2)	3.266×10^3	1.723×10^3	1.055×10^3	1.724×10^4	5.575×10^2
CPE_{diff}	4.088×10^{-6}	5.946×10^{-6}	6.768×10^{-6}	–	4.395×10^{-6}
n_{diff}	0.4656	0.5912	0.6181	–	0.4279
R_{diff} (ohm·cm^2)	4.712×10^3	1.071×10^3	7.738×10^2	–	6.668×10^2
W (S sec^5 cm^{-2})	–	–	–	3.570×10^{-6}	–
CPE_{dl}	4.147×10^{-6}	6.825×10^{-6}	9.367×10^{-6}	5.039×10^{-7}	1.281×10^{-5}
n_{dl}	0.7901	0.7824	0.7060	0.8125	0.6852
R_{ct} (ohm cm^2)	5.518×10^4	2.182×10^4	1.314×10^4	8.456×10^4	7.750×10^3

Table S5. EIS fitting results of Zn-2 immersed in the SBF solution for different time durations based on the EC.

Immersion time	3 day	7 day	14 day	28 day	56 day
CPE_c	1.704×10^{-8}	8.981×10^{-8}	4.113×10^{-7}	1.521×10^{-6}	2.823×10^{-8}
n_c	0.6277	0.8160	0.7722	0.9422	0.6007
R_c (ohm cm^2)	8.512×10^3	4.694×10^3	1.703×10^3	1.477×10^3	2.093×10^4
CPE_{diff}	3.415×10^{-7}	5.657×10^{-6}	1.212×10^{-5}	1.490×10^{-5}	–
n_{diff}	0.9172	0.4333	0.3290	0.5566	–
R_{diff} (ohm cm^2)	5.922×10^4	5.263×10^3	3.951×10^3	1.885×10^3	–
W ($S \cdot sec^5$ cm^{-2})	–	–	–	–	4.79×10^{-6}
CPE_{dl}	8.401×10^{-7}	3.168×10^{-6}	5.353×10^{-6}	7.734×10^{-6}	4.985×10^{-7}
n_{dl}	0.8890	0.8484	0.7020	0.7864	0.4760
R_{ct} (ohm cm^2)	9.279×10^4	7.632×10^4	2.067×10^4	1.016×10^4	6.025×10^5

Table S6. EIS fitting results of Zn-3 immersed in the SBF solution for different time durations based on the EC.

Immersion time	3 day	7 day	14 day	28 day	56 day
CPE_c	5.868×10^{-9}	5.622×10^{-8}	2.015×10^{-7}	1.036×10^{-6}	3.572×10^{-6}
n_c	0.6079	0.7398	0.9201	0.3539	0.7964
R_c (ohm cm^2)	3.484×10^4	9.981×10^3	3.158×10^3	2.206×10^3	1.371×10^3
CPE_{diff}	1.282×10^{-7}	2.852×10^{-6}	3.333×10^{-6}	5.760×10^{-6}	6.058×10^{-6}
n_{diff}	1.0000	0.8257	0.8029	0.5729	0.8589
R_{diff} (ohm cm^2)	4.803×10^{-7}	1.028×10^5	7.194×10^4	5.795×10^4	1.079×10^4
CPE_{dl}	2.940×10^{-3}	1.967×10^{-6}	2.312×10^{-6}	3.218×10^{-6}	6.120×10^{-6}
n_{dl}	0.9733	0.3572	0.4196	0.6845	0.3681
R_{ct} (ohm cm^2)	1.246×10^5	9.543×10^4	4.255×10^4	3.308×10^4	1.390×10^4

Table S7. Elemental concentrations on the surface of the AZ31B alloy and MAO coatings immersed in SBF solution for 56 days determined by EDS.

Concentrations (at%)	AZ31B	Zn-0	Zn-1	Zn-2	Zn-3
C	12.46	13.07	11.09	11.68	11.77
O	53.51	51.25	51.68	52.73	53.98
F	–	0.78	1.02	1.14	1.18
Mg	19.64	19.07	21.78	21.84	20.01
Al	2.83	2.11	0.54	0.37	0.28
Si	0.40	0.70	0.24	0.82	0.55
P	5.96	6.99	9.67	8.25	9.03
Cl	0.14	0.14	0.05	0.10	0.04
Ca	4.68	5.59	2.88	1.72	1.26
Zn	0.39	0.29	1.05	1.36	1.90